

DEEP EIGENSPACE NETWORK AND ITS APPLICATION TO PARAMETRIC NON-SELFADJOINT EIGENVALUE PROBLEMS*

HAOQIAN LI[†], JIGUANG SUN[‡], AND ZHIWEN ZHANG[§]

Abstract. We consider operator learning for efficiently solving parametric non-selfadjoint eigenvalue problems. To overcome the spectral instability and mode switching inherent in non-selfadjoint operators, we introduce a hybrid framework that learns the stable invariant eigensubspace mapping rather than individual eigenfunctions. We proposed a Deep Eigenspace Network (DEN) architecture integrating Fourier Neural Operators, geometry-adaptive POD bases, and explicit banded cross-mode mixing mechanisms to capture complex spectral dependencies on unstructured meshes. We apply DEN to the parametric non-selfadjoint Steklov eigenvalue problem and provide theoretical proofs for the Lipschitz continuity of the eigensubspace with respect to the parameters. In addition, we derive error bounds for the reconstruction of the eigenspace. Numerical experiments validate DEN’s high accuracy and zero-shot generalization capabilities across different discretizations.

Key words. Operator learning, Non-selfadjoint Steklov eigenvalue problems.

1. Introduction. Deep learning approaches have gained increasing attention for solving eigenvalue problems of partial differential equations. Early efforts primarily focused on solving fixed, often high-dimensional instances. For example, various architectures based on the Deep Ritz method, semigroup approaches, or Tensor Neural Networks have been developed to approximate single or multiple eigenpairs in high-dimensional settings [16, 21, 18, 34, 4]. Notably, regarding the precision of multiple eigenpair computation, Dai et al. [13] achieved highly accurate results for elliptic operators by ingeniously integrating classical subspace iteration methods with PINNs.

Shifting the focus from solving single instances to operator learning, i.e., learning the mapping from system parameters to spectral properties, Li et al. [20] successfully utilized Fourier Neural Operators (FNO) and CNNs to predict the eigenvalues and eigenfunctions of the Laplacian on variable domains. Chang et al. [10] employed PINNs to track the continuous evolution of eigenfunctions with respect to shape deformations. However, these works either address self-adjoint problems or rely on physics-informed loss functions that may face challenges in the non-selfadjoint case.

Most existing deep learning-based eigensolvers focus on optimizing solutions for a specific, fixed parameter configuration. In contrast, our objective is to achieve operator learning, enabling the prediction of spectral properties for a certain class of parameter inputs without retraining. While operator learning models may not match the absolute numerical precision of classical methods such as finite elements [33], they offer a compelling trade-off: once trained, they provide real-time inference with accuracy that is sufficient. This is a desired property in many-query tasks such

*Submitted to the editors DATE.

Funding: JS was partially supported by NSF Grant DMS-2109949 and SIMONS Foundation Collaboration Grant 711922. ZZ was partially supported by the National Natural Science Foundation of China (Project 92470103), the Hong Kong RGC grant (Project 17304324), an R&D Funding Scheme from the HKU-SCF FinTech Academy, the Outstanding Young Researcher Award of HKU (2020-21), and Seed Funding for Strategic Interdisciplinary Research Scheme 2021/22 (HKU).

[†]Department of Mathematics, The University of Hong Kong, Pokfulam Road, Hong Kong SAR, China. lihaoqianlhq@connect.hku.hk.

[‡]Corresponding author. Department of Mathematical Sciences, Michigan Technological University, Houghton, MI 49931, U.S.A. jiguangs@mtu.edu.

[§]Corresponding author. Department of Mathematics, The University of Hong Kong, Pokfulam Road, Hong Kong SAR, China. AND Materials Innovation Institute for Life Sciences and Energy (MILES), HKU-SIRI, Shenzhen, P. R. China. zhangzw@hku.hk

as inverse scattering problems.

In this paper, we consider the construction of operator learning framework to approximate the parameter-to-solution mapping for non-selfadjoint eigenvalue problems. Non-selfadjoint nature leads to a fundamental challenge: direct regression of individual eigenfunctions is numerically intractable due to the inherent spectral instability of non-selfadjoint operators. As described by matrix perturbation theory [32], spectral clustering and mode crossings, common in this regime, cause individual eigenvectors to rotate rapidly or switch indices, rendering the mapping $n(x) \mapsto u_i$ highly non-smooth or discontinuous. To overcome this, we pivot to learning the **invariant eigenspace**, which remains stable even when individual vectors within the cluster fluctuate. By employing a neural operator to predict the stable subspace and subsequently utilizing the Rayleigh-Ritz procedure to recover specific eigenpairs, our hybrid approach effectively synergizes the learnability of continuous subspace mappings with the rigorous numerical robustness of classical linear algebra.

Among the burgeoning operator learning paradigms [28, 23, 24, 26, 35, 11, 27], the Fourier Neural Operator (FNO) [22] has garnered significant attention for its computational efficiency and its exceptional ability to capture non-local dependencies via spectral convolutions. However, applying FNO to the non-selfadjoint eigenvalue problem on unstructured meshes necessitates two key architectural challenges: the specific mathematical structure of the operator and the domain geometry.

First, in contrast to translation-invariant operators where frequency modes are approximately decoupled, non-selfadjoint operators are characterized by intrinsic spectral couplings. To capture these complex inter-modal dependencies, which extend beyond the diagonal structure of standard spectral layers, we identify the need for a mechanism that explicitly models the interaction between distinct frequency modes. Second, to accommodate the non-uniform discretizations typical of Finite Element Methods (FEM) while retaining global receptive field advantage over local message-passing Graph Neural Networks (GNNs)[12], it is essential to generalize the spectral transform beyond the uniform-grid restrictions of the FFT.

Synthesizing these requirements, we introduce the **Deep Eigenspace Network (DEN)**. Other than the fixed Fourier basis, we use a geometry-adaptive basis that naturally handles unstructured data. Specifically, we demonstrate that for stationary problems, the Proper Orthogonal Decomposition (POD) basis derived from the output snapshots constitutes the theoretically optimal subspace. Furthermore, to model the spectral couplings efficiently, we augment the spectral convolution layer with explicit cross-mode connections, parameterized via low-rank banded matrices. This design enables DEN to capture intricate off-diagonal dependencies while maintaining the computational efficiency characteristic of spectral operators.

We apply DEN to the parametric Steklov eigenvalue problem. Distinguished by the presence of the spectral parameter in the boundary conditions rather than the domain, the Steklov eigenvalue problem constitutes a fundamental class of spectral problems in mathematical physics [19]. Historically, this formulation has been pivotal in modeling a wide array of physical phenomena. Prominent examples include the study of surface water waves, the dynamics of mechanical oscillators immersed in viscous fluids, and the analysis of vibration modes for structures in contact with incompressible fluids [8, 9, 19].

While the theoretical properties of Steklov eigenvalue problems have been extensively studied, the development of robust numerical methods has gained momentum only relatively recently. A wide variety of discretization techniques have been proposed, including isoparametric finite element methods (FEM) [2], virtual element

methods [29], non-conforming FEM [30], spectral-Galerkin methods [1], and advanced adaptive or multilevel schemes [5, 17]. However, the vast majority of these contributions differ from our focus in one critical aspect: they are restricted to **self-adjoint** operators.

In contrast, the **non-selfadjoint** Steklov eigenvalue problem, which arises naturally in the modeling of inhomogeneous absorbing media for inverse scattering [7], remains significantly under-explored. To the best of our knowledge, the theoretical foundation was primarily addressed in the seminal work by Bramble and Osborn [6], yet their analysis assumed uniform ellipticity and did not provide numerical realizations. The scarcity of literature is partly due to the computational challenges involved. Discretizing non-selfadjoint operators leads to non-Hermitian generalized eigenvalue problems (GEPs). Unlike Hermitian problems where robust solvers abound, non-Hermitian GEPs are notoriously difficult to solve efficiently. Although iterative methods such as the Arnoldi, Lanczos, and Jacobi-Davidson algorithms [3] are available, they often suffer from slow convergence and high memory consumption, and their performance is "far from satisfactory" [31], especially when the distribution of eigenvalues is unknown a priori. Recently, to mitigate these difficulties, Liu et al. [25] proposed applying the Spectral Indicator Method (SIM) to compute non-selfadjoint Steklov eigenvalues, providing a rigorous tool to calculate eigenvalues in specific regions of the complex plane.

The remainder of this paper is organized as follows. In Section 2, we introduce the architecture of the proposed Deep Eigenspace Network (DEN). Section 3 presents the specific subspace learning framework for parametric Steklov eigenvalue problems, including the loss formulation on the Grassmann manifold and the hybrid Rayleigh-Ritz reconstruction procedure. In Section 4, we provide a rigorous theoretical analysis regarding the stability of the eigensubspace with respect to parameter perturbations and deriving explicit error bounds for the reconstructed eigenvalues. Section 5 reports numerical experiments to demonstrate the accuracy, efficiency, zero-shot generalization capabilities, and robustness of our method with respect to different magnitudes of input parameters. Finally, Section 6 concludes.

2. Deep Eigenspace Network. In this section, we begin with an overview of the Fourier Neural Operator (FNO). Subsequently, motivated by the specific requirements of predicting eigensubspaces for non-selfadjoint Steklov problems, we identify the limitations of the standard FNO. This analysis serves as the foundation for our proposed architecture, the Deep Eigenspace Network (DEN), which introduces multifaceted improvements to enhance performance in this domain. Figure 1 demonstrates the structure of proposed DEN.

2.1. Structure of the Fourier Neural Operator. The Fourier Neural Operator (FNO) represents a significant class of operator-learning architectures. By alternating between the spatial and Fourier domains, FNOs capture global, non-local interactions far more efficiently than standard convolutional or recurrent models, which are inherently limited by their local receptive fields [22].

Let $\mathbf{n}(x) \in \mathbb{R}^{d_{\text{in}} \times w \times h}$ denote the discretized input function (e.g., the variable coefficient parameter), where d_{in} , w , and h denote the input channel dimension, width, and height, respectively. Let $\mathbf{y}(x) \in \mathbb{R}^{d_{\text{out}} \times w \times h}$ denote the target output (e.g., the target eigensubspace projection). The architecture of the FNO proceeds as follows:

1. **Lifting Layer \mathcal{P} :** This is a pointwise linear transformation that maps the input into a higher-dimensional latent representation d_0 , formally expressed

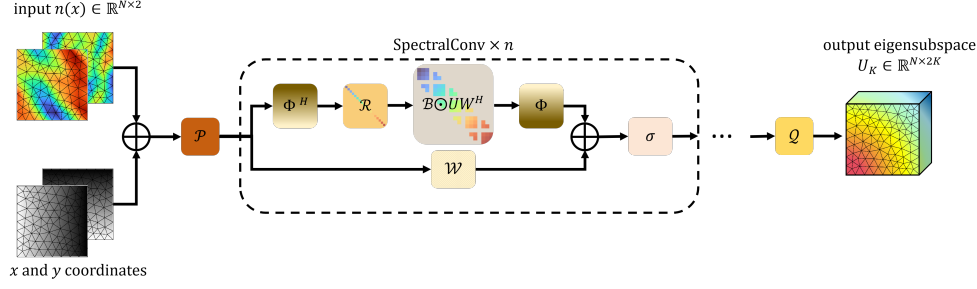


Fig. 1: Structure of Deep Eigenspace Network.

as:

$$(2.1) \quad \mathbf{z}^{(0)} = \mathcal{P}(\mathbf{n}(x)) \in \mathbb{R}^{d_0 \times w \times h}.$$

2. **Iterative Spectral Convolution Layers:** The network processes the latent representation through a sequence of spectral convolution blocks. For $l = 0, \dots, L - 1$, the update rule is given by:

$$(2.2) \quad \mathbf{z}^{(l+1)} = \sigma \left(\mathcal{F}^{-1} \left[\mathcal{R} \cdot \left(\mathcal{F} \mathbf{z}^{(l)} \right) \right] + \mathcal{W} \mathbf{z}^{(l)} + \mathbf{b}^{(l)} \right),$$

where:

- \mathcal{F} and \mathcal{F}^{-1} denote the 2-D discrete Fourier transform and its inverse, respectively.
- \mathcal{W} is a local linear operator (pointwise 1×1 convolution) acting in the physical space, and $\mathbf{b}^{(l)}$ is a learnable bias.
- σ is a nonlinear activation function (e.g., GeLU or ReLU).
- \mathcal{R} represents the learnable spectral filter. Let $\hat{\mathbf{z}}^{(l)} = \mathcal{F} \mathbf{z}^{(l)}$. The operation $\mathcal{R} \cdot \hat{\mathbf{z}}^{(l)}$ performs channel-mixing in the frequency domain. Considering the truncated Fourier modes, let K be the total number of preserved modes. For each mode $m \in \{1, \dots, K\}$, the output at the $(l + 1)$ -th layer, $\hat{\mathbf{z}}_{c_{in}, m}^{(l+1)}$, is computed as:

$$(2.3) \quad \hat{\mathbf{z}}_{c_{out}, m}^{(l+1)} = \sum_{c_{in}=1}^{d_l} R_{c_{in}, c_{out}, m}^{(l)} \hat{\mathbf{z}}_{c_{in}, m}^{(l)},$$

where $R^{(l)} \in \mathbb{C}^{d_l \times d_{l+1} \times K}$ is a learnable complex-valued tensor.

The summation of the spectral branch and the local residual branch (\mathcal{W}) enables the block to integrate global frequency information with local spatial features.

3. **Projection Layer \mathcal{Q} :** Finally, a pointwise linear map projects the high-dimensional features back to the target dimension d_{out} , yielding the final output $\mathbf{y} = \mathcal{Q}(\mathbf{z}^{(L)})$.

Our network architecture, the Deep Eigenspace Network (DEN), is designed by adapting the powerful spectral learning paradigm of the FNO to the specific mathematical structure of non-selfadjoint eigenvalue problems. While FNO has demonstrated remarkable success in learning solution operators for PDEs, the distinct characteristics of the Steklov problem, namely, the non-diagonal nature of the operator

and the geometric complexity of the domain, necessitate two key architectural evolutions: explicit spectral coupling and geometry-adaptive basis representation.

Modeling Spectral Couplings via Cross-Mode Mixing. The standard FNO employs a spectral convolution layer that performs efficient dense operations across channel dimensions but treats each frequency mode independently. This design is highly effective for translation-invariant operators where the Fourier modes are approximately decoupled. However, non-selfadjoint operators are inherently characterized by strong interactions between different eigenmodes (spectral couplings). To capture these complex dependencies, we extend the spectral convolution mechanism by introducing explicit cross-mode connections. Rather than relying solely on spatial residual layers to approximate these interactions, we directly model the off-diagonal structure in the frequency domain. To maintain computational efficiency, we parameterize these interactions using low-rank banded matrices, achieving a balance between representational capacity and computational cost (detailed in Sections 2.2 and 2.4).

Geometry-Adaptive Spectral Learning. The second adaptation addresses the discretization context. In scientific computing workflows utilizing the Finite Element Method (FEM), data is naturally defined on non-uniform and unstructured meshes. While Graph Neural Networks (GNNs) offer a pathway for unstructured data, they rely on local message passing, which often struggles to capture long-range spectral dependencies due to the "over-smoothing" phenomenon. To retain the global receptive field of spectral methods while accommodating arbitrary geometries, we adopt the Generalized Spectral Operator framework [11, 27]. The core idea is to generalize the Fourier transform by replacing the fixed sinusoidal basis with a geometry-adaptive orthogonal basis $\Psi \in \mathbb{R}^{N \times K}$. The generalized spectral convolution layer is thus formulated as:

$$(2.4) \quad \mathbf{z}^{(l+1)} = \sigma \left(\Psi \left(\mathcal{R} \cdot (\Psi^H \mathbf{z}^{(l)}) \right) + \mathcal{W} \mathbf{z}^{(l)} + \mathbf{b} \right),$$

where the projection $\Psi^H \mathbf{z}^{(l)}$ maps the physical signal to a generalized coefficient space.

Optimality of the POD Basis. The choice of the basis Ψ is pivotal. While the graph Laplacian eigenfunctions are a generic choice for arbitrary geometries, our focus on stationary problems with fixed discretizations allows for a more targeted approach. In Section 2.3, we demonstrate that the Proper Orthogonal Decomposition (POD) basis, derived directly from the snapshot matrix of the target outputs, constitutes the theoretically optimal linear subspace for reconstruction. By utilizing $\text{POD}(\mathbf{Y})$ as the spectral basis, DEN effectively aligns the network's latent representation with the intrinsic manifold of the Steklov eigenfunctions.

It is worth noting that our approach shares similarities with the Generalized Spectral Operator (GSO) and Proper Orthogonal Decomposition Neural Operator (PODNO) frameworks proposed by Cheng et al. [11]. They utilized various POD strategies, including mixing input/output snapshots or aggregating snapshots across time steps. While their work explores a broader class of time-dependent PDEs, our focus on the stationary eigenvalue problem allows for a more specific theoretical assertion: $\text{POD}(\mathbf{Y})$ provides the optimal linear subspace for reconstruction in the L^2 sense. This does not contradict the findings of Cheng et al.; rather, it complements them. In time-dependent settings, the solution manifold evolves, rendering a static $\text{POD}(\mathbf{Y})$ basis potentially suboptimal or misaligned with the dynamics at specific time t . However, for our static mapping problem, the output manifold is fixed, making the target-derived POD basis the theoretically optimal choice for aligning the output manifold. It is precisely their pioneering work on GSOs that motivated our

investigation into basis optimality for the Steklov problem.

2.2. Enhancing Expressivity via Cross-Mode Mixing. Let Ψ be an orthogonal transformation basis and A be the target linear operator acting on the physical domain. Its spectral representation is given by a transformation $A_\Psi := \Psi^{-1}A\Psi$. For general PDEs involving variable coefficients, complex boundary conditions, or non-translation-invariant phenomena, A_Ψ is generally *non-diagonal*; energy spreads across frequencies, inducing non-trivial cross-mode coupling.

To address the limitations of diagonal approximations, we introduce a *cross-mode mixing operator*. While channel mixing remains specific to the architecture, we focus here on the spectral mixing. We introduce a matrix $M \in \mathbb{C}^{K \times K}$ that couples spectral modes:

$$(2.5) \quad \mathbf{u}_{\text{coupled}} = \mathbf{u}_{\text{diag}}M.$$

In the simplest formulation (shared across channels), the enhanced spectral convolution becomes:

$$(2.6) \quad \mathbf{y} = \Psi M (R \cdot \Psi^H \mathbf{x}).$$

This formulation expands the hypothesis space from diagonal operators to the full space of linear operators on the span of Ψ .

PROPOSITION 2.1 (Irreducible Error of Diagonal Approximations). *Let $A_\Psi \in \mathbb{C}^{K \times K}$ be the spectral representation of a target operator. Let $\mathcal{D} \subset \mathbb{C}^{K \times K}$ be the subspace of diagonal matrices, and let $\mathcal{M} = \mathbb{C}^{K \times K}$ be the space of arbitrary matrices. Define the approximation errors for the diagonal and full models as:*

$$(2.7) \quad \varepsilon_{\mathcal{D}} = \min_{D \in \mathcal{D}} \|A_\Psi - D\|_F, \quad \text{and} \quad \varepsilon_{\mathcal{M}} = \min_{M \in \mathcal{M}} \|A_\Psi - M\|_F,$$

where $\|\cdot\|_F$ denotes the Frobenius norm.

If A_Ψ possesses non-zero off-diagonal entries, then:

$$(2.8) \quad \varepsilon_{\mathcal{D}} > 0 = \varepsilon_{\mathcal{M}}.$$

Specifically, the diagonal model suffers from an irreducible error equal to the energy of the off-diagonal terms.

Proof. The space of matrices $\mathbb{C}^{K \times K}$ admits an orthogonal decomposition with respect to the Frobenius inner product: $\mathbb{C}^{K \times K} = \mathcal{D} \oplus \mathcal{D}^\perp$, where \mathcal{D}^\perp is the subspace of hollow matrices (matrices with zero diagonal). Since $A_\Psi \in \mathbb{C}^{K \times K}$, we can uniquely decompose it as:

$$(2.9) \quad A_\Psi = \text{diag}(A_\Psi) + \text{off}(A_\Psi),$$

where $\text{diag}(A_\Psi) \in \mathcal{D}$ and $\text{off}(A_\Psi) \in \mathcal{D}^\perp$. Consider the objective function for the diagonal estimator:

$$(2.10) \quad \|A_\Psi - D\|_F^2 = \|(\text{diag}(A_\Psi) - D) + \text{off}(A_\Psi)\|_F^2.$$

By the orthogonality of \mathcal{D} and \mathcal{D}^\perp , this expands to:

$$(2.11) \quad \|\text{diag}(A_\Psi) - D\|_F^2 + \|\text{off}(A_\Psi)\|_F^2.$$

The minimum is achieved when $D = \text{diag}(A_\Psi)$, yielding the residual error:

$$(2.12) \quad \varepsilon_{\mathcal{D}} = \|\text{off}(A_\Psi)\|_F.$$

Therefore, if A_Ψ is not strictly diagonal (i.e., $\|\text{off}(A_\Psi)\|_F > 0$), the diagonal parameterization incurs a strictly positive irreducible error. Conversely, since $A_\Psi \in \mathcal{M}$, the full model can set $M = A_\Psi$, resulting in $\varepsilon_{\mathcal{M}} = 0$. \square

This proposition rigorously demonstrates that adding cross-mode interaction is necessary to eliminate representation error whenever the physics dictates spectral coupling.

2.3. On the Basis Selection. We analyze the impact of basis selection on the performance of Fourier Neural Operators (FNO) equipped with a cross-mode mixing layer. Specifically, we compare an *Aligned Basis* (e.g., $\text{POD}(Y)$) against an *Entangled Basis* (e.g., $\text{POD}(X, Y)$).

We postulate that even if the architecture allows for dense cross-mode interactions (M), using an entangled basis is suboptimal due to (1) reduction in effective parameter capacity and (2) ill-conditioning of the optimization landscape.

- Let $\mathcal{Z} \cong \mathbb{R}^K$ be the spectral feature space of dimension K .
- Let $\mathcal{S}_Y \subset \mathcal{Z}$ be the **Target Subspace** (signal manifold) with $\dim(\mathcal{S}_Y) = d_Y$.
- Let $\mathcal{S}_\perp \subset \mathcal{Z}$ be the **Irrelevant Subspace** (noise manifold) with $\dim(\mathcal{S}_\perp) = d_\perp$, such that $\mathcal{Z} = \mathcal{S}_Y \oplus \mathcal{S}_\perp$.
- Let the ideal physical dynamics be represented by a linear operator $D : \mathcal{S}_Y \rightarrow \mathcal{S}_Y$.
- Let the spectral layer operation be defined as $z_{out} = M z_{in}$, where $M \in \mathbb{R}^{K \times K}$ is the learnable cross-mode mixing matrix.

DEFINITION 2.2 (Entangled Basis). A basis set $\{\phi_k\}_{k=1}^K$ is called *entangled* if the basis vectors are linear combinations of signal and noise components. Specifically, for an input state $z \in \mathcal{Z}$ represented in this basis:

$$(2.13) \quad z = z_Y + z_\perp, \quad \text{where } z_Y \in \mathcal{S}_Y, z_\perp \in \mathcal{S}_\perp.$$

In an entangled basis (like $\text{POD}(X, Y)$), the energy of the irrelevant component is non-negligible, i.e., $\|z_\perp\| \gg 0$. In an aligned basis (like $\text{POD}(Y)$), $z_\perp \approx 0$.

THEOREM 2.3 (Effective Rank Contraction). Let the learning objective be to approximate the dynamics D on \mathcal{S}_Y while suppressing the noise from \mathcal{S}_\perp . That is, the learned operator M must satisfy:

1. **Denoising Condition:** $M z_\perp = 0, \quad \forall z_\perp \in \mathcal{S}_\perp$.
2. **Evolution Condition:** $M z_Y \approx D z_Y, \quad \forall z_Y \in \mathcal{S}_Y$.

If $\text{rank}(M) \leq r_{max}$, then the effective rank available to approximate the physical dynamics D is bounded by:

$$(2.14) \quad \text{rank}(M|_{\mathcal{S}_Y}) \leq r_{max} - d_\perp$$

Proof. Let $\mathcal{N}(M)$ denote the null space (kernel) of M . The Denoising Condition implies that the irrelevant subspace must be mapped to zero:

$$(2.15) \quad \mathcal{S}_\perp \subseteq \mathcal{N}(M)$$

Therefore, the dimension of the null space must satisfy:

$$(2.16) \quad \dim(\mathcal{N}(M)) \geq \dim(\mathcal{S}_\perp) = d_\perp$$

By the Rank-Nullity Theorem, for the operator M defined on the domain \mathcal{Z} of dimension K (assuming effective domain is covered by rank r_{max} logic):

$$(2.17) \quad \text{rank}(M) + \dim(\mathcal{N}(M)) = \dim(\text{Dom}(M))$$

Considering the active degrees of freedom allowed by the low-rank constraint r_{max} , the dimension of the image space $\text{Im}(M)$ is at most r_{max} . Since M must annihilate \mathcal{S}_\perp , the subspace available to represent the image of \mathcal{S}_Y is orthogonal to the components consumed by the null space requirement. Thus, the effective rank for the signal is:

$$(2.18) \quad \text{rank}_{eff} = \text{rank}(M) - \dim(\text{rank consumed by } \mathcal{S}_\perp) \leq r_{max} - d_\perp$$

If d_\perp is large (high entanglement), the model suffers from a *capacity deficit*, leading to underfitting of the physical dynamics D . \square

Following the establishment of the effective rank contraction caused by entangled bases, we now identify the optimal basis configuration. We posit that to maximize the representational capacity of the spectral layer, the basis must be strictly aligned with the geometry of the target signal manifold.

THEOREM 2.4 (Optimality of the Output-Aligned Basis). *Let $Y \in \mathbb{R}^{N \times d_n}$ be the snapshot matrix of the target physical states (the solution manifold), and let $C_Y = \mathbb{E}[yy^\top]$ be the covariance operator of the target signals. Assume the spectral mixing layer seeks a rank- K approximation of the operator output. The projection error energy:*

$$(2.19) \quad \mathcal{E}(\Psi) = \mathbb{E}_{y \sim \mathcal{S}_Y} [\|y - \Psi\Psi^H y\|_2^2]$$

is minimized if and only if the basis V spans the same subspace as the first K principal components of Y (denoted as $\text{POD}(Y)$). Consequently, under this basis, the dimension of the irrelevant subspace vanishes ($d_\perp = 0$), and the effective rank is maximized:

$$(2.20) \quad \text{rank}(M|_{\mathcal{S}_Y}) = \text{rank}(M).$$

Proof. The proof follows from the variational characterization of the singular value decomposition (Eckart-Young-Mirsky theorem[14]).

This result theoretically justifies decoupling the input and output bases. While an entangled basis attempts to span both the input condition space and the solution space, the operator learning task is strictly directional ($X \rightarrow Y$). By aligning the spectral layer's codomain with $\text{POD}(Y)$, we ensure the matrix M focuses solely on the destination manifold.

2.4. Banded Low-Rank Parameterization. While Proposition 2.1 suggests that a dense mixing matrix M minimizes representation error, directly parameterizing M as a full matrix introduces significant optimization difficulties. In practice, operators arising from physical systems exhibit specific spectral structures, namely, energy concentration and local spectral coupling. Ignoring these structures leads to poor convergence and overfitting. To address this, we propose a **Banded Low-Rank (BLR)** parameterization.

Low-Rank Property of the Spectral Operator. The first structural prior is the low effective rank of the target operator in the POD basis. By construction, the POD basis vectors $\Psi = \{\psi_k\}_{k=1}^K$ are ordered by their energy contribution to the dataset. Consequently, the output of the physical operator, $y = \mathcal{A}(x)$, resides primarily in the subspace spanned by the first few dominant modes.

Mathematically, this implies that the spectral representation $A_\Psi = \Psi^H A \Psi$ is *numerically low-rank*. Although A_Ψ may theoretically be full-rank, its singular values decay rapidly. A full-rank parameterization of M is therefore over-parameterized, learning noise correlations in the tail of the spectrum rather than physical dynamics. We thus approximate the mixing operator using a low-rank factorization:

$$(2.21) \quad M_{LR} = UW^H, \quad \text{where } U, W \in \mathbb{C}^{K \times r}, r \ll K.$$

Optimization Stability via Banded Constraints. The second, and critical, structural prior concerns the *ordering* of the spectrum. A standard low-rank factorization $M_{LR} = UW^H$ is globally coupled; at initialization, it connects every frequency mode to every other mode with non-zero probability. This causes two optimization issues:

1. **Spectral Pollution:** Random initialization allows high-frequency noise to propagate directly into dominant low-frequency modes (from high indices to low indices). This disrupts the coarse-grained physical features early in training.
2. **Optimization Landscape:** The model is forced to expend early training iterations “unlearning” these unphysical long-range couplings to restore the correct spectral hierarchy, leading to a rugged optimization landscape.

To stabilize training, we introduce a banded constraint. Physical energy transfer typically occurs between spectrally adjacent modes (e.g., energy cascade in fluids) rather than arbitrary non-local jumps. We enforce this locality by applying a band mask \mathcal{B} to the low-rank matrix, ensuring that interactions are restricted to a bandwidth b along the diagonal.

Mathematical Formulation. We define the binary mask matrix $\mathcal{B} \in \{0, 1\}^{K \times K}$ as:

$$(2.22) \quad \mathcal{B}_{ij} = \begin{cases} 1 & \text{if } |i - j| \leq b, \\ 0 & \text{otherwise,} \end{cases}$$

where b is a hyperparameter controlling the spectral interaction bandwidth. The final cross-mode mixing operator M is defined as the Hadamard product of the mask and the low-rank component:

$$(2.23) \quad M_{BLR} = \mathcal{B} \odot (UW^H).$$

where \odot denotes the element-wise multiplication, i.e., Hadamard product.

This formulation combines the best of both worlds: the low-rank structure UW^H captures the dominant subspace of the operator, while the banded mask \mathcal{B} imposes an inductive bias that respects the spectral ordering, preventing noise injection and accelerating convergence.

3. Methodology. In this section, we formally define the Steklov eigenvalue problem and analyze the specific challenges introduced by the non-selfadjoint nature of the operator. We then introduce our proposed subspace learning framework and the corresponding loss function. Following the prediction of the eigensubspace, we detail the Rayleigh-Ritz procedure used to recover the eigenvalues and eigenfunctions. Finally, the data generation process is described.

3.1. Problem Setup.

3.1.1. The Non-Selfadjoint Steklov Eigenvalue Problem. Let $\Omega \subset \mathbb{R}^2$ be a bounded domain with a Lipschitz boundary $\partial\Omega$. We consider the generalized Steklov eigenvalue problem governing the acoustic field in a medium with a variable refractive index. The problem is formulated as finding the eigenpair (λ, u) such that:

$$(3.1) \quad \begin{cases} \Delta u + k^2 n(x)u = 0 & \text{in } \Omega, \\ \frac{\partial u}{\partial \nu} + \lambda u = 0 & \text{on } \partial\Omega, \end{cases}$$

where ν denotes the outward unit normal vector, k is the wavenumber, and $n(x) = n_1(x) + i \frac{n_2(x)}{k}$ is the refractive index parameter, $n_1(x) > 0$, $n_2(x) \geq 0$ are bounded smooth functions.

The variational (weak) formulation corresponding to (3.1) is to find $\lambda \in \mathbb{C}$ and $u \in H^1(\Omega) \setminus \{0\}$ such that:

$$(3.2) \quad a(u, v) = \lambda b(u, v), \quad \forall v \in H^1(\Omega),$$

where the sesquilinear forms $a(\cdot, \cdot)$ and $b(\cdot, \cdot)$ are defined as:

$$(3.3) \quad a(u, v) = - \int_{\Omega} \nabla u \cdot \nabla \bar{v} \, dx + k^2 \int_{\Omega} n(x) u \bar{v} \, dx, \quad b(u, v) = \int_{\partial\Omega} u \bar{v} \, ds.$$

A critical challenge in this work arises when the parameter $n(x)$ is complex-valued (modeling absorbing media). In this regime, the operator becomes **non-selfadjoint**. This introduces several theoretical and numerical complexities compared to the self-adjoint case:

- **Complex Spectrum:** The eigenvalues λ are complex-valued ($\lambda \in \mathbb{C}$), rendering the natural ordering (e.g., $\lambda_1 \geq \lambda_2 \geq \dots$) inapplicable. Sorting is typically performed based on the modulus $|\lambda|$ or real part, which is susceptible to reordering under perturbation.
- **Non-Orthogonality:** The eigenfunctions $\{u_i\}$ are no longer mutually orthogonal with respect to the standard inner product. While a biorthogonality relation exists with the adjoint problem, the lack of self-orthogonality complicates projection-based methods.
- **Invalidity of Min-Max Principles:** In the context of self-adjoint eigenvalue problems (where $n(x)$ is real), the classical Rayleigh quotient

$$(3.4) \quad \mathcal{R}(u) = \frac{a(u, u)}{b(u, u)}$$

provides a variational characterization of the spectrum. The eigenvalues can be determined via the Courant-Fischer min-max principle:

$$(3.5) \quad \lambda_k = \min_{V_k \subset H^1, \dim(V_k)=k} \max_{u \in V_k, u \neq 0} \mathcal{R}(u).$$

This property is instrumental in many physics-informed learning frameworks. For instance, Dai et al. [13] leverage this property to construct loss functions based on minimizing the Rayleigh quotient, thereby training neural networks to find eigenpairs without labeled data.

However, in our non-selfadjoint Steklov setting, the sesquilinear form $a(u, u)$ becomes complex-valued due to the complex refractive index $n(x)$. Consequently, the Rayleigh quotient $\mathcal{R}(u)$ maps to the complex plane \mathbb{C} , which is

not an ordered field. The concepts of minimization and maximization are mathematically ill-defined for complex numbers. Furthermore, even if one considers the modulus $|\mathcal{R}(u)|$, the stationary points of the magnitude of the Rayleigh quotient do not generally correspond to the eigenvalues of the non-selfadjoint operator. This fundamental lack of variational bounds renders standard optimization-based spectral solvers ineffective, necessitating the supervised operator learning approach adopted in this work.

3.1.2. Discrete Formulation and The Curse of Mode Crossing. Applying the Finite Element Method (FEM) discretization leads to the generalized matrix eigenvalue problem:

$$(3.6) \quad \mathbf{A}(n)\mathbf{x} = \lambda\mathbf{B}\mathbf{x},$$

where \mathbf{x} is the coefficient vector of the eigenfunction. The matrices are defined as $\mathbf{A}(n) = -\mathbf{S} + k^2\mathbf{M}_n$ and $\mathbf{B} = \mathbf{M}_{\partial\Omega}$, where \mathbf{S} is the stiffness matrix, \mathbf{M}_n is the domain mass matrix weighted by $n(x)$, and $\mathbf{M}_{\partial\Omega}$ is the boundary mass matrix.

Our objective is to learn the operator $\mathcal{G} : n(x) \mapsto \{(\lambda_i, u_i)\}_{i=1}^K$, mapping the parameter $n(x)$ to the first K eigenpairs (sorted by modulus). A naive approach would be to train neural operators to regress λ_i and u_i directly.

However, preliminary investigations reveal a fundamental difficulty: while eigenvalues generally exhibit continuous dependence on parameters, the eigenfunctions are notoriously difficult to predict directly. This difficulty stems from the behavior of non-selfadjoint spectra under perturbation. As described by matrix perturbation theory [32], when eigenvalues form a **cluster** or undergo **crossing** (e.g., $|\lambda_i| \approx |\lambda_{i+1}|$ as $n(x)$ varies), the corresponding eigenvectors become extremely sensitive to perturbations. The eigenvectors may rotate rapidly or discontinuously within the invariant subspace spanned by the cluster. Consequently, the mapping $n(x) \mapsto u_i$ becomes highly non-smooth or even discontinuous due to index switching, necessitating complex mode-matching algorithms and extremely large training datasets to resolve.

To overcome the instability of individual eigenvectors, we pivot to learning the **eigensubspace**. Although individual eigenvectors are unstable near crossings, the invariant subspace associated with a cluster of eigenvalues is stable, provided the cluster is separated from the rest of the spectrum (refer to Section 4.1 for a detailed proof of subspace stability).

Therefore, instead of predicting unstable eigenvectors, we propose to learn the mapping from $n(x)$ to eigensubspace $\mathcal{U}_K = \text{span}\{u_1, \dots, u_K\}$. Once the subspace is accurately predicted, the individual eigenpairs are recovered via the Rayleigh-Ritz procedure, which solves the small-scale projected eigenvalue problem, as introduced in Section 3.3. This hybrid approach combines the differentiability of subspace mappings with the numerical robustness of classical linear algebra.

3.2. Subspace Learning Framework. Recent advancements by Fanaskov et al. [15] have introduced a rigorous framework for subspace regression using deep learning, demonstrating its potential in parametric eigenvalue problems. Building upon this foundation, we formalize our learning objective as follows.

Let $\mathcal{V} \subset \mathbb{C}^N$ be the target eigensubspace spanned by the first k_V eigenfunctions, represented by the matrix $\mathbf{V} \in \mathbb{C}^{N \times k_V}$. Our goal is to train a neural operator to predict a subspace \mathcal{U} , represented by $\mathbf{U} \in \mathbb{C}^{N \times k_U}$, such that \mathcal{V} is embedded within \mathcal{U} . We allow the predicted dimension k_U to be equal to or greater than the target dimension (i.e., $k_V \leq k_U$). The condition $\mathcal{V} \subseteq \mathcal{U}$ ensures that the true eigenvectors can be recovered as linear combinations of the basis vectors of \mathcal{U} .

To achieve this, the loss function $\mathcal{L}(\mathbf{U}, \mathbf{V})$ must satisfy two fundamental algebraic properties:

- (i) **Basis Invariance:** The loss should depend only on the subspaces spanned by the matrices, not on their specific basis representations. That is, for any invertible matrices $\mathbf{S} \in \mathbb{C}^{k_U \times k_U}$ and $\mathbf{T} \in \mathbb{C}^{k_V \times k_V}$:

$$(3.7) \quad \mathcal{L}(\mathbf{US}, \mathbf{VT}) = \mathcal{L}(\mathbf{U}, \mathbf{V}).$$

- (ii) **Inclusion Monotonicity:** The loss should be non-negative, reaching zero if and only if the inclusion condition is met:

$$(3.8) \quad \mathcal{L}(\mathbf{U}, \mathbf{V}) \geq 0, \quad \text{and} \quad \mathcal{L}(\mathbf{U}, \mathbf{V}) = 0 \iff \text{span}(\mathbf{V}) \subseteq \text{span}(\mathbf{U}).$$

Note that when $k_U > k_V$, the loss is asymmetric, i.e., $\mathcal{L}(\mathbf{U}, \mathbf{V}) \neq \mathcal{L}(\mathbf{V}, \mathbf{U})$.

Fanaskov et al. proposed two loss functions satisfying these criteria. The first, denoted as \mathcal{L}_1 , measures the orthogonality defect between the subspaces:

$$(3.9) \quad \mathcal{L}_1(\mathbf{U}, \mathbf{V}) = k_V - \|\mathbf{Q}_V^H \mathbf{Q}_U\|_F^2,$$

where \mathbf{Q}_U and \mathbf{Q}_V are the orthonormal bases obtained from \mathbf{U} and \mathbf{V} (e.g., via QR decomposition), and $\|\cdot\|_F$ denotes the Frobenius norm. The second, \mathcal{L}_2 , is a stochastic projection loss:

$$(3.10) \quad \mathcal{L}_2(\mathbf{U}, \mathbf{V}; \mathbf{z}) = \min_{\mathbf{x}} \|\mathbf{U}\mathbf{x} - \mathbf{Q}_V \mathbf{z}\|_2^2,$$

where $\mathbf{z} \in \mathbb{C}^{k_V}$ is a random vector with zero mean and identity covariance. Theoretically, it has been shown that \mathcal{L}_2 is an estimator of the projection error:

$$(3.11) \quad \mathbb{E}_{\mathbf{z}}[\mathcal{L}_2(\mathbf{U}, \mathbf{V}; \mathbf{z})] = \mathcal{L}_1(\mathbf{U}, \mathbf{V}) = \frac{1}{2} \|\mathbf{P}_U - \mathbf{P}_V\|_F^2 - \frac{k_U - k_V}{2},$$

where \mathbf{P}_U and \mathbf{P}_V are the orthogonal projection matrices onto \mathcal{U} and \mathcal{V} , respectively.

While \mathcal{L}_2 scales better computationally for high-dimensional subspaces ($k_U \gg 1$), it introduces stochastic variance during training. In our context, as discussed in Section 4.1, the eigensubspaces associated with spectral clusters are relatively stable and low-dimensional. Therefore, we do not require a massive over-parameterization of k_U . Given this stability, the deterministic loss \mathcal{L}_1 provides a more direct and precise gradient signal for optimization. Thus, we adopt \mathcal{L}_1 as our objective function.

We employ the previously described DEN architecture as the operator approximator. To handle the complex-valued nature of the Steklov problem within standard deep learning frameworks, we adopt a real-valued tensor representation.

Input Representation: The complex parameter $n(x) = n_r(x) + i n_i(x)$ is stacked with the spatial coordinates. For a mesh with N nodes, the input is formatted as a tensor of shape $[4, N]$, where the four channels correspond to the real part of n , the imaginary part of n , and the x, y coordinates of the mesh nodes. Explicitly including coordinates aids the network in capturing geometry-dependent spectral features.

Output and Orthogonalization: The network outputs a real tensor of shape $[2k_U, N]$. The first k_U channels represent the real parts of the basis vectors, while the subsequent k_U channels represent the imaginary parts. Let $\tilde{\mathbf{U}}_{\text{out}}$ denote this raw output. We reconstruct the complex matrix $\mathbf{U} \in \mathbb{C}^{N \times k_U}$ via:

$$(3.12) \quad \mathbf{U}_{:,j} = (\tilde{\mathbf{U}}_{\text{out}})_{j,:} + i(\tilde{\mathbf{U}}_{\text{out}})_{j+k_U,:}, \quad j = 1, \dots, k_U.$$

To ensure numerical stability and satisfy the input requirements of \mathcal{L}_1 , we apply a differentiable QR decomposition to \mathbf{U} during the forward pass:

$$(3.13) \quad \mathbf{U} = \mathbf{Q}_U \mathbf{R}_U.$$

The resulting unitary matrix \mathbf{Q}_U is then passed to the loss function (3.9) for training.

3.3. Eigenpair Reconstruction via Rayleigh-Ritz Method. Once the predictive network DEN provides the approximate eigensubspace basis $\mathbf{Q}_U \in \mathbb{C}^{N \times k_U}$ (orthonormalized via QR decomposition), we employ the Rayleigh-Ritz procedure to extract the specific eigenpairs. This step can be viewed as a Galerkin projection of the full fine-scale problem onto the low-dimensional subspace spanned by \mathbf{Q}_U .

Given the parameter-dependent mass matrix \mathbf{M}_n (constructed from the input $n(x)$) and the pre-computed constant matrices \mathbf{S} and $\mathbf{M}_{\partial\Omega}$, the full system matrices are $\mathbf{A}(n) = -\mathbf{S} + k^2 \mathbf{M}_n$ and $\mathbf{B} = \mathbf{M}_{\partial\Omega}$. The Rayleigh-Ritz method proceeds in three steps:

1. **Projection (Subspace Assembly):** We project the full matrices onto the predicted subspace to form the reduced stiffness and mass matrices:

$$(3.14) \quad \hat{\mathbf{A}} = \mathbf{Q}_U^H \mathbf{A}(n) \mathbf{Q}_U, \quad \hat{\mathbf{B}} = \mathbf{Q}_U^H \mathbf{B} \mathbf{Q}_U,$$

where $\hat{\mathbf{A}}, \hat{\mathbf{B}} \in \mathbb{C}^{k_U \times k_U}$ are small, dense matrices.

2. **Solving the Reduced Problem:** We solve the generalized eigenvalue problem for the reduced system:

$$(3.15) \quad \hat{\mathbf{A}} \mathbf{w}_j = \mu_j \hat{\mathbf{B}} \mathbf{w}_j, \quad j = 1, \dots, k_U.$$

Since $k_U \ll N$ (typically $k_U \sim 10^1$ while $N \sim 10^4$), this step is computationally negligible compared to solving the full system.

3. **Lifting (Reconstruction):** The Ritz values μ_j serve as approximations for the exact eigenvalues λ_j . The corresponding Ritz vectors are lifted back to the full space to approximate the eigenfunctions:

$$(3.16) \quad \tilde{u}_j = \mathbf{Q}_U \mathbf{w}_j.$$

This procedure ensures that the reconstructed eigenfunctions \tilde{u}_j strictly reside within the predicted subspace \mathcal{U} and optimally satisfy the variational formulation restricted to that subspace.

The primary motivation for this hybrid approach stems from the computational bottleneck inherent in the Finite Element Method (FEM). In standard FEM workflows, the assembly of the system matrices is relatively fast, scaling linearly with the number of elements. The computational dominance lies in solving the Generalized Eigenvalue Problem (GEP).

While the system matrices \mathbf{A} and \mathbf{B} are typically sparse, allowing for efficient $\mathcal{O}(N)$ matrix-vector products, standard solvers rely on iterative Krylov subspace methods (e.g., Arnoldi or Lanczos iterations). A critical limitation of these methods is their initialization: they typically commence with a random starting vector. Due to this lack of prior knowledge, the solver requires a substantial number of iterations to "filter out" the unwanted spectral components and converge to the target eigenspace. Consequently, although the asymptotic complexity per iteration is linear, the large constant factor, determined by the number of iterations required for convergence, makes the eigensolver the overwhelming computational cost in the pipeline.

In contrast, our proposed pipeline bypasses this iterative search, drastically reducing the online computational burden:

- **Matrix Assembly:** The parameter-dependent matrix $\mathbf{A}(n)$ is constructed via an update of \mathbf{M}_n followed by a sparse addition. This involves only basic sparse matrix arithmetic (e.g., two matrix multiplications and one addition in our implementation), which is computationally inexpensive.
- **Projection Cost:** The formation of the reduced matrices $\hat{\mathbf{A}}$ and $\hat{\mathbf{B}}$ requires projecting the sparse full matrices onto the predicted basis \mathbf{Q}_U . This operation involves sparse-dense matrix multiplications, with a complexity of approximately $\mathcal{O}(N \cdot k_U^2)$.
- **Solving Cost:** Solving the reduced GEP involves dense matrices of size $k_U \times k_U$, entailing a cost of $\mathcal{O}(k_U^3)$.

Given that the subspace dimension k_U is a small constant fixed by the network architecture (independent of the mesh size N), the total complexity of our method effectively scales linearly, $\mathcal{O}(N)$, with a very small constant factor. This represents a significant speedup over classical iterative solvers, particularly for tasks requiring repeated evaluations such as inverse design or uncertainty quantification.

Our approach shares conceptual roots with classical Krylov subspace methods (e.g., Arnoldi or Lanczos iterations). Classical methods generate a search subspace iteratively by repeatedly applying the operator to a starting vector (e.g., $\mathcal{K}_m = \text{span}\{v, \mathbf{A}^{-1}\mathbf{B}v, \dots\}$). While rigorous, these iterations require solving large linear systems at every step, which is expensive.

Our method can be interpreted as a **”Data-Driven Preconditioning”** or a **”Direct Subspace Prediction”**. Instead of building the subspace iteratively via costly matrix-vector products, the DEN network predicts the converged invariant subspace directly from the parameters in a single forward pass. The Rayleigh-Ritz step then acts as a final **”polishing”** mechanism, ensuring that the spectral approximations are mathematically consistent with the underlying operators \mathbf{A} and \mathbf{B} .

3.4. Dataset Generation. To evaluate the robustness of our method on non-selfadjoint operators, we generate a diverse dataset of physically plausible, complex-valued refractive-index profiles $k^2 n(x)$. For simplicity, we choose $k = 1$. The complex parameter is defined as $n(x) = n_r(x) + in_i(x)$.

We synthesize the spatial variability of $n(x)$ by superposing random sinusoidal modes. To ensure independence between the real and imaginary components, we generate two distinct random fields, $g_r(x)$ and $g_i(x)$. Generally, a random field $g(x)$ is constructed via the following expansion: for integers $m \leq j \leq M$,

$$(3.17) \quad g(x) = \sum_{j=m}^M \beta^{-j} \left(a_j \sin(2\pi f_j u(x; \alpha_j) + \theta_j) + b_j \sin(2\pi f_j v(x; \alpha_j) + \varphi_j) \right),$$

where $x = (x, y)$, and the coordinate rotation is given by:

$$(3.18) \quad u(x; \alpha) = \frac{x \cos \alpha + y \sin \alpha}{2}, \quad v(x; \alpha) = \frac{x \sin \alpha + y \cos \alpha}{2}.$$

For each mode j , the parameters are sampled as:

$$(3.19) \quad a_j, b_j \sim \mathcal{N}(0, 1), \quad \theta_j, \varphi_j, \alpha_j \sim \mathcal{U}(0, 2\pi),$$

with spatial frequency set to $f_j = j$. The scalar $\beta \in (0, 1)$ controls the spectral decay, favoring low-frequency structures to mimic smooth background media perturbed by fine local variations.

The final complex parameter $n(x)$ is obtained by independently sampling coefficients for g_r and g_i , followed by a min-max normalization to map them into physically meaningful ranges:

$$(3.20) \quad n(x) = \mathcal{T}_{[n_r^{\min}, n_r^{\max}]}(g_r(x)) + i \cdot \mathcal{T}_{[n_i^{\min}, n_i^{\max}]}(g_i(x)),$$

where $\mathcal{T}_{[a,b]}(\cdot)$ denotes the linear scaling operator. In our experiments, we set both the real range and the imaginary range to $[1.0, 5.0]$ for simplicity.

Unlike methods that rely on rasterized images (pixels), our problem is defined on a fixed unstructured triangular mesh to better capture complex geometries and conform to standard Finite Element Method (FEM) workflows. The domain Ω is discretized into a mesh with N nodes. Consequently, each realization of the parameter $n(x)$ is represented as a complex vector $\mathbf{n} \in \mathbb{C}^N$. Similarly, the target eigenfunctions are stored as vectors $\mathbf{u} \in \mathbb{C}^N$.

We generate a total of 2000 samples (1600 for training and 400 for testing). To balance computational efficiency with approximation accuracy, the mesh resolution is chosen such that $N \approx 1500$ nodes. This resolution is sufficient to resolve the oscillatory nature of the target eigenfunctions while keeping the training cost of the graph-based neural operators manageable. Figure 2 visualizes the real and imaginary parts of selected samples from the dataset.

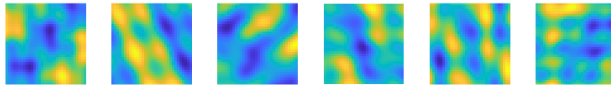


Fig. 2: Samples of generated $n(x)$

4. Learnability and Error Analysis.

4.1. Eigensubspace Stability. We consider the generalized eigenvalue problem

$$(4.1) \quad Ax = \lambda Bx,$$

and a contour $\Gamma \subset \mathbb{C}$ enclosing a cluster Λ_0 consisting of K eigenvalues. We introduce the following assumptions.

ASSUMPTION 4.1. *The contour Γ separates Λ_0 from the rest of the spectrum, and*

$$(4.2) \quad \text{dist}(\Gamma, \sigma(A, B) \setminus \Lambda_0) = \delta > 0.$$

ASSUMPTION 4.2. *The resolvent along Γ is bounded by*

$$(4.3) \quad R_\Gamma := \sup_{z \in \Gamma} \|(Bz - A)^{-1}\| < \infty.$$

ASSUMPTION 4.3. *The perturbation matrix M satisfies the smallness condition*

$$(4.4) \quad \|M\| R_\Gamma < 1.$$

LEMMA 4.4 (Resolvent Stability). *Under Assumptions 4.1–4.3, the following hold:*

1. *For every perturbation matrix M satisfying Assumption 4.3, the matrix $Bz - A - M$ is invertible for all $z \in \Gamma$, and*

$$(4.5) \quad \sup_{z \in \Gamma} \|(Bz - A - M)^{-1}\| \leq \frac{R_\Gamma}{1 - R_\Gamma \|M\|}.$$

2. *The resolvent difference satisfies*

$$(4.6) \quad \|(Bz - A)^{-1} - (Bz - A - M)^{-1}\| \leq R_\Gamma^2 \|M\| + O(\|M\|^2), \quad z \in \Gamma.$$

Proof. For notational convenience, let $T(z) = Bz - A$. According to Assumption 4.2, $T(z)$ is invertible for all $z \in \Gamma$, and $\|T(z)^{-1}\| \leq R_\Gamma$.

1. We write the perturbed matrix as

$$(4.7) \quad Bz - A - M = T(z) - M = T(z) (I - T(z)^{-1}M).$$

Let $E = T(z)^{-1}M$. Using the submultiplicativity of the matrix norm and Assumption 4.3, we have

$$(4.8) \quad \|E\| \leq \|T(z)^{-1}\| \|M\| \leq R_\Gamma \|M\| < 1.$$

Since $\|E\| < 1$, the matrix $I - E$ is invertible, and its inverse can be expressed via the Neumann series $(I - E)^{-1} = \sum_{j=0}^{\infty} E^j$. Consequently, $Bz - A - M$ is invertible, and its inverse is given by

$$(4.9) \quad (Bz - A - M)^{-1} = (I - E)^{-1}T(z)^{-1}.$$

Taking the norm, we obtain

$$(4.10) \quad \begin{aligned} \|(Bz - A - M)^{-1}\| &\leq \|(I - E)^{-1}\| \|T(z)^{-1}\| \\ &\leq \frac{1}{1 - \|E\|} R_\Gamma \\ &\leq \frac{R_\Gamma}{1 - R_\Gamma \|M\|}. \end{aligned}$$

2. Using the factorization from Part 1 and the Neumann expansion for $(I - E)^{-1}$, we have

$$(4.11) \quad \begin{aligned} (Bz - A - M)^{-1} &= \left(I + E + \sum_{j=2}^{\infty} E^j \right) T(z)^{-1} \\ &= T(z)^{-1} + ET(z)^{-1} + \left(\sum_{j=2}^{\infty} E^j \right) T(z)^{-1}. \end{aligned}$$

Recall that $(Bz - A)^{-1} = T(z)^{-1}$. The difference is

$$(4.12) \quad (Bz - A - M)^{-1} - (Bz - A)^{-1} = T(z)^{-1}MT(z)^{-1} + \mathcal{R}(z),$$

where $\mathcal{R}(z) = \sum_{j=2}^{\infty} (T(z)^{-1}M)^j T(z)^{-1}$. The norm of the first order term is bounded by:

$$(4.13) \quad \|T(z)^{-1}MT(z)^{-1}\| \leq \|T(z)^{-1}\|^2 \|M\| \leq R_\Gamma^2 \|M\|.$$

The remainder term $\mathcal{R}(z)$ is of order $O(\|M\|^2)$ because

$$(4.14) \quad \|\mathcal{R}(z)\| \leq \sum_{j=2}^{\infty} (R_{\Gamma}\|M\|)^j R_{\Gamma} = \frac{(R_{\Gamma}\|M\|)^2 R_{\Gamma}}{1 - R_{\Gamma}\|M\|} = O(\|M\|^2),$$

provided that $R_{\Gamma}\|M\|$ is sufficiently small. Combining these yields

$$(4.15) \quad \|(Bz - A)^{-1} - (Bz - A - M)^{-1}\| \leq R_{\Gamma}^2\|M\| + O(\|M\|^2). \quad \square$$

Remark 4.5 (Practical Implications). The significance of Lemma 4.4 in the context of our numerical experiments is threefold:

1. **Configuration:** In our study, we define the reference operator as $A = -S + M_{\bar{n}}$, where \bar{n} represents the statistical mean of the refractive index samples in the dataset. The target spectral set $\Lambda_0 = \{\lambda_1, \dots, \lambda_{12}\}$ comprises the first 12 eigenvalues, which constitute the first five complete eigenvalue clusters.
2. **Spectral Isolation:** We have empirically verified that Assumptions 4.1 and 4.2 hold for this configuration. Crucially, all samples in our dataset satisfy the smallness condition (Assumption 4.3). Consequently, Lemma 4.4 guarantees that the contour Γ remains strictly within the resolvent set for every perturbed operator $A(n)$. This implies that no eigenvalues from outside Λ_0 (i.e., λ_{13}, \dots) can cross Γ to mix with the target cluster. Thus, the dimensionality of the eigensubspace enclosed by Γ remains invariant across the entire dataset.
3. **Uniform Stability:** Equation 4.5 establishes a uniform bound on the resolvent norm along the fixed contour Γ for all admissible perturbations. This uniform boundedness is not merely a technical detail; it serves as a necessary condition for the following theorem, providing the foundation to prove the Lipschitz continuity of the map from the parameter $n(x)$ to the eigensubspace projection.

THEOREM 4.6 (Stability of Riesz Projections). *Let M_{n_1} be a perturbation matrix satisfying Assumption 4.3, and define*

$$(4.16) \quad R_{\Gamma, n_1} := \sup_{z \in \Gamma} \|(Bz - A - M_{n_1})^{-1}\|,$$

which is finite by Lemma 4.4. Let M_{n_2} be another perturbation matrix, and set $\Delta M := M_{n_2} - M_{n_1}$. Assume that

$$(4.17) \quad \|\Delta M\| R_{\Gamma, n_1} < 1.$$

Let P_{n_i} denote the Riesz spectral projection onto the K eigenvalues of

$$(4.18) \quad (A + M_{n_i})x = \lambda Bx, \quad i = 1, 2.$$

Then the projections satisfy the stability estimate

$$(4.19) \quad \|P_{n_1} - P_{n_2}\| \leq \frac{|\Gamma|}{2\pi} R_{\Gamma, n_1}^2 \|\Delta M\| + O(\|\Delta M\|^2).$$

Furthermore, if M_{n_1} and M_{n_2} arise from material parameters $n_1(x)$ and $n_2(x)$, then

$$(4.20) \quad \|P_{n_1} - P_{n_2}\| \leq C\|n_1 - n_2\|.$$

Proof. We proceed in two steps: first establishing the stability bound with respect to the matrix perturbation ΔM , and second relating this to the material parameter difference $\|n_1 - n_2\|$.

1. *Stability with respect to matrix perturbation.* By definition, the Riesz spectral projection P_{n_i} associated with the pair $(A + M_{n_i}, B)$ corresponding to the eigenvalues inside Γ is given by

$$(4.21) \quad P_{n_i} = \frac{1}{2\pi i} \oint_{\Gamma} (Bz - A - M_{n_i})^{-1} B \, dz, \quad i = 1, 2.$$

Let $T_1(z) = Bz - A - M_{n_1}$ and $T_2(z) = Bz - A - M_{n_2}$. We are interested in estimating the norm of the difference:

$$(4.22) \quad P_{n_1} - P_{n_2} = \frac{1}{2\pi i} \oint_{\Gamma} (T_1(z)^{-1} - T_2(z)^{-1}) B \, dz.$$

We view $T_2(z)$ as a perturbation of $T_1(z)$:

$$(4.23) \quad T_2(z) = (Bz - A - M_{n_1}) - (M_{n_2} - M_{n_1}) = T_1(z) - \Delta M.$$

By Assumption 4.3 and Lemma 4.4, $T_1(z)$ is invertible for $z \in \Gamma$ with

$$(4.24) \quad \sup_{z \in \Gamma} \|T_1(z)^{-1}\| = R_{\Gamma, n_1}.$$

Factoring out $T_1(z)$, we write

$$(4.25) \quad T_2(z) = T_1(z) (I - T_1(z)^{-1} \Delta M).$$

Since $\|\Delta M\| R_{\Gamma, n_1} < 1$, the inverse $T_2(z)^{-1}$ can be expanded using the Neumann series:

$$(4.26) \quad \begin{aligned} T_2(z)^{-1} &= (I - T_1(z)^{-1} \Delta M)^{-1} T_1(z)^{-1} \\ &= \left(I + T_1(z)^{-1} \Delta M + \sum_{j=2}^{\infty} (T_1(z)^{-1} \Delta M)^j \right) T_1(z)^{-1} \\ &= T_1(z)^{-1} + T_1(z)^{-1} \Delta M T_1(z)^{-1} + \mathcal{R}(z), \end{aligned}$$

where the remainder term satisfies $\|\mathcal{R}(z)\| = O(\|\Delta M\|^2)$. Substituting this expansion into the integral for the projection difference, we obtain

$$(4.27) \quad P_{n_1} - P_{n_2} = -\frac{1}{2\pi i} \oint_{\Gamma} (T_1(z)^{-1} \Delta M T_1(z)^{-1} + \mathcal{R}(z)) B \, dz.$$

Taking the norm and using the boundedness of B (absorbed into the implied constants or assuming normalized B), we have

$$(4.28) \quad \begin{aligned} \|P_{n_1} - P_{n_2}\| &\leq \frac{|\Gamma|}{2\pi} \sup_{z \in \Gamma} \|T_1(z)^{-1} \Delta M T_1(z)^{-1}\| \|B\| + O(\|\Delta M\|^2) \\ &\leq \frac{|\Gamma|}{2\pi} \left(\sup_{z \in \Gamma} \|T_1(z)^{-1}\| \right)^2 \|\Delta M\| \|B\| + O(\|\Delta M\|^2) \\ &\leq C_B \frac{|\Gamma|}{2\pi} R_{\Gamma, n_1}^2 \|\Delta M\| + O(\|\Delta M\|^2). \end{aligned}$$

This confirms the first estimate (where $\|B\|$ is typically $O(1)$).

2. *Relation to material parameters.* We now establish the bound in terms of $\|n_1 - n_2\|$. Based on the finite element discretization description, the matrix M_n is assembled from local element contributions. Let $\mathcal{T}_h = \{K_e\}_{e=1}^{M_e}$ be the triangulation. The parameter n is represented by the vector $\mathbf{n} \in \mathbb{R}^{3 \times M_e}$ containing values at the midpoints of the edges of each element.

The construction of M_n is described by the linear operation:

$$(4.29) \quad M_n^{(e)} = \text{mat} \left((\mathbf{w}^T \cdot \mathbf{n}_e) \frac{|K_e|}{3} \right),$$

where $\mathbf{n}_e \in \mathbb{R}^3$ are the values for element e , \mathbf{w}^T is a fixed weight matrix of size 9×3 , and $\text{mat}(\cdot)$ reshapes the resulting vector into a local 3×3 element matrix. The global matrix M_n is the assembly (sum) of these local matrices:

$$(4.30) \quad M_n = \sum_{e=1}^{M_e} \mathcal{A}_e(M_n^{(e)}),$$

where \mathcal{A}_e is the assembly operator. Since the mapping from the parameter vector \mathbf{n} to the local matrix entries is linear (multiplication by constant weights $\mathbf{y}\mathbf{y}^T$ and area factors), and the global assembly is linear, the mapping $\Phi : \mathbf{n} \mapsto M_n$ is a linear operator between finite-dimensional vector spaces.

Consequently, Φ is Lipschitz continuous. There exists a constant C_{mesh} depending on the mesh geometry (via element areas and weights) such that

$$(4.31) \quad \|\Delta M\| = \|M_{n_1} - M_{n_2}\| = \|\Phi(\mathbf{n}_1) - \Phi(\mathbf{n}_2)\| = \|\Phi(\mathbf{n}_1 - \mathbf{n}_2)\| \leq C_{\text{mesh}} \|\mathbf{n}_1 - \mathbf{n}_2\|.$$

Substituting this into the stability estimate derived in Part 1 yields

$$(4.32) \quad \|P_{n_1} - P_{n_2}\| \leq C' R_{\Gamma, n_1}^2 C_{\text{mesh}} \|n_1 - n_2\| + O(\|n_1 - n_2\|^2),$$

which implies

$$(4.33) \quad \|P_{n_1} - P_{n_2}\| \leq C \|n_1 - n_2\|,$$

for a constant $C > 0$. □

The theoretical results derived above provide a rigorous justification for the learnability of the proposed mapping. First, Lemma 4.4 guarantees **Uniform Spectral Isolation** across the entire dataset. It ensures that the contour Γ consistently separates the target cluster from the rest of the spectrum for all admissible samples, preventing any external eigenfunctions from "polluting" the target subspace. This establishes the consistency of the learning target. Second, Theorem 4.6 establishes the **Lipschitz continuous dependence** of the eigensubspace projection on the refractive index parameter n . Combining these findings with the fact that the admissible parameters $n(x)$ reside in a bounded compact set (as defined in Section 3.4), we conclude that the mapping from the parameter space to the Grassmann manifold is both well-defined and continuous. According to the Universal Approximation Theorems for neural operators, such continuous mappings on compact domains are intrinsically learnable, thereby providing the theoretical guarantee for our data-driven approach.

4.2. Eigenvalue Reconstruction Error Bound.

ASSUMPTION 4.7 (Setup and Subspace Alignment). *Let $A, B \in \mathbb{C}^{n \times n}$ define a generalized eigenvalue problem. Let \mathcal{V} be a K -dimensional subspace (the target eigenspace) and \mathcal{U} be an approximation of dimension K . Let $V \in \mathbb{C}^{n \times K}$ and $U \in \mathbb{C}^{n \times K}$ be orthonormal bases for \mathcal{V} and \mathcal{U} , respectively ($V^*V = U^*U = I_K$).*

We assume U is the specific basis for \mathcal{U} that minimizes the distance to V . That is, U satisfies the Procrustes condition:

$$(4.34) \quad \|U - V\|_2 = \min_{Q \in \mathbb{C}^{K \times K}, Q^*Q = I} \|U_{\text{raw}}Q - V\|_2,$$

where U_{raw} is any initial orthonormal basis for \mathcal{U} . The misalignment between the subspaces is quantified by the sine of the canonical angles:

$$(4.35) \quad \sin \Theta(\mathcal{U}, \mathcal{V}) := \|(I - P_V)P_U\|_2 = \|(I - P_U)P_V\|_2,$$

where $P_V = VV^*$ and $P_U = UU^*$.

LEMMA 4.8 (Matrix Projection Error Bound). *Under Assumption 4.7, define the projected matrices $A_V = V^*AV$, $B_V = V^*BV$ (and similarly for U). Then, the deviation of the projected matrices is linearly bounded by the subspace misalignment. Specifically,*

$$(4.36) \quad \|A_U - A_V\|_2 \leq 2\sqrt{2}\|A\|_2 \sin \Theta,$$

$$(4.37) \quad \|B_U - B_V\|_2 \leq 2\sqrt{2}\|B\|_2 \sin \Theta.$$

Proof. Consider the difference $A_U - A_V$. By adding and subtracting U^*AV , we obtain:

$$(4.38) \quad \begin{aligned} A_U - A_V &= U^*AU - V^*AV \\ &= U^*A(U - V) + (U^* - V^*)AV. \end{aligned}$$

Taking the spectral norm and applying the triangle inequality yields:

$$(4.39) \quad \|A_U - A_V\|_2 \leq \|U\|_2\|A\|_2\|U - V\|_2 + \|U - V\|_2\|A\|_2\|V\|_2.$$

Since U and V are orthonormal, $\|U\|_2 = \|V\|_2 = 1$. Thus,

$$(4.40) \quad \|A_U - A_V\|_2 \leq 2\|A\|_2\|U - V\|_2.$$

From the theory of canonical angles (e.g., [32]), the distance between optimally aligned bases is bounded by the gap metric:

$$(4.41) \quad \|U - V\|_2 \leq \sqrt{2} \sin \Theta.$$

Substituting this into the norm inequality completes the proof for A . The derivation for B is identical. \square

LEMMA 4.9 (Spectral Variation for Diagonalizable Pencils). *Let (M, N) be a regular matrix pair of size $K \times K$ that is diagonalizable. That is, there exist non-singular matrices X, Y such that $Y^*MX = \Lambda$ and $Y^*NX = \Omega$ are diagonal. Let $\{\lambda_i = \Lambda_{ii}/\Omega_{ii}\}$ be the generalized eigenvalues. Define the eigenvalue condition number for the i -th mode as:*

$$(4.42) \quad \nu_i := \frac{\|x_i\|_2\|y_i\|_2}{\sqrt{|\Lambda_{ii}|^2 + |\Omega_{ii}|^2}},$$

where x_i, y_i are the i -th columns of X and Y .

Consider a perturbed pair $(\tilde{M}, \tilde{N}) = (M + E, N + F)$. The spectral variation, defined as the maximum distance from a true eigenvalue to the set of perturbed eigenvalues $\{\tilde{\lambda}_j\}$, satisfies:

$$(4.43) \quad \text{sv}_{(M,N)}[(\tilde{M}, \tilde{N})] := \max_i \min_j |\tilde{\lambda}_j - \lambda_i| \leq \left(\max_i \nu_i \right) \sqrt{\|E\|_2^2 + \|F\|_2^2}.$$

Proof. Corollary 2.8 of [32] gives

$$(4.44) \quad \text{sv}_{(M,N)}[(\tilde{M}, \tilde{N})] \leq \left(\max_i \nu_i \right) \|[E \ F]\|_2.$$

The bound follows by

$$(4.45) \quad \|[E \ F]\|_2^2 = \|EE^* + FF^*\|_2 \leq \|EE^*\|_2 + \|FF^*\|_2 = \|E\|_2^2 + \|F\|_2^2. \quad \square$$

THEOREM 4.10 (Linear Convergence of Ritz Values). *Consider the generalized eigenvalue problem $Ax = \lambda Bx$. Suppose the target eigenspace \mathcal{V} corresponds to a cluster of K eigenvalues that is separated from the rest of the spectrum. Let (A_V, B_V) be the exact restriction and (A_U, B_U) be the Rayleigh-Ritz approximation as defined in Assumption 4.7.*

Assume (A_V, B_V) is diagonalizable and has a maximal condition number $\nu_{\max} = \max_i \nu_i$. Then, the error in the Ritz values $\{\mu_j\}_{j=1}^K$ relative to the exact eigenvalues $\{\lambda_i\}_{i=1}^K$ is controlled linearly by the subspace misalignment $\sin \Theta$:

$$(4.46) \quad \text{sv}_{(A_V, B_V)}[(A_U, B_U)] \leq 2\sqrt{2}\nu_{\max} \cdot \sin \Theta \sqrt{\|A\|_2^2 + \|B\|_2^2}.$$

Proof. We interpret the Ritz pair (A_U, B_U) as a perturbation of the exact projected pair (A_V, B_V) . Let

$$(4.47) \quad E = A_U - A_V, \quad F = B_U - B_V.$$

By Lemma 4.9, the spectral variation is bounded by:

$$(4.48) \quad \text{sv} \leq \nu_{\max} \sqrt{\|A_U - A_V\|_2^2 + \|B_U - B_V\|_2^2}.$$

Applying the bounds from Lemma 4.8:

$$(4.49) \quad \|A_U - A_V\|_2 \leq 2\sqrt{2}\|A\|_2 \sin \Theta, \quad \|B_U - B_V\|_2 \leq 2\sqrt{2}\|B\|_2 \sin \Theta.$$

Substituting these into the spectral variation bound:

$$(4.50) \quad \begin{aligned} \text{sv}_{(A_V, B_V)}[(A_U, B_U)] &\leq \nu_{\max} \sqrt{(2\sqrt{2}\|A\|_2 \sin \Theta)^2 + (2\sqrt{2}\|B\|_2 \sin \Theta)^2} \\ &= \nu_{\max} \cdot 2\sqrt{2} \sin \Theta \sqrt{\|A\|_2^2 + \|B\|_2^2} \end{aligned}$$

Thus, the error in the generalized eigenvalues is $O(\sin \Theta)$, i.e., of the same order as the subspace error. \square

	Parameter	Value
Network settings	Number of spectral convolution layers	4
	Number of hidden channels	32
	Dimension of POD basis	240
	Rank of mode-mixing matrix	32
	Bandwith of mode-mixng matrix	5
	Activation function	GeLU
Training settings	Batch size	32
	Initial learning rate	0.01
	Number of epochs	201
	Learning rate decay step and rate	(20, 0.8)
	Optimizer	Adam
	Weight decay	1e-6

Table 1: Network and training settings.

5. Numerical Experiments. In this section, we present a comprehensive evaluation of the proposed DEN framework. We begin by detailing the experimental setup, training hyperparameters, and the evaluation metrics used to quantify performance. Subsequently, we report the numerical results, demonstrating that our method achieves high accuracy in predicting both eigensubspaces and reconstructed eigenpairs. Furthermore, we investigate the **zero-shot generalization** capability of our model by evaluating its performance when transferring the predicted subspace from a source mesh to a target mesh with a different resolution, highlighting the discretization-independent nature of the operator learning approach. Secondly, we extend our evaluation to investigate the robustness of the DEN framework under varying magnitudes of physical parameters, controlled by wavenumber k . We will demonstrate that while our method achieves exceptional precision in low-frequency regimes, it also maintains competitive accuracy in more challenging high-frequency settings through the adoption of a subspace embedding strategy. Finally, we conducted an ablation study and numerically demonstrated the optimality of the proposed network structure.

5.1. Settings and Evaluation Metrics. Our proposed DEN architecture is implemented using the PyTorch framework. The specific hyperparameters for the network architecture and the training procedure are summarized in Table 5.1.

The experiments were conducted with a single NVIDIA GeForce RTX 3090 GPU (24GB VRAM). Thanks to the efficient design of the DEN and the subspace learning strategy, the computational cost is minimal. The training process for the entire dataset converges rapidly, requiring approximately 3 to 4 minutes for 201 epochs. This efficiency stands in stark contrast to the data generation process using standard FEM, which takes hours, highlighting the significant speedup achieved by the surrogate model.

To provide a comprehensive assessment of the DEN model, we evaluate its performance across three distinct dimensions: the spectral accuracy (eigenvalues), the geometric accuracy (eigensubspaces), and the basis representation accuracy (eigenfunctions).

1. *Eigenvalue Metrics.* Since the eigenvalues λ_k are complex-valued, we assess the errors based on their moduli and positions in the complex plane. For the k -th

eigenvalue across the test dataset (of size N_{test}), we employ the following metrics:

- **Mean Absolute Error (MAE):** Measures the average absolute deviation.

$$(5.1) \quad \text{MAE}_k = \frac{1}{N_{test}} \sum_{i=1}^{N_{test}} |\lambda_k^{(i)} - \hat{\lambda}_k^{(i)}|,$$

where $\lambda_k^{(i)}$ and $\hat{\lambda}_k^{(i)}$ are the ground truth and predicted eigenvalues for the i -th sample, respectively. This metric reflects the direct numerical precision.

- **Coefficient of Determination (R^2):** Measures the proportion of variance explained by the model.

$$(5.2) \quad R_k^2 = 1 - \frac{\sum_{i=1}^{N_{test}} |\lambda_k^{(i)} - \hat{\lambda}_k^{(i)}|^2}{\sum_{i=1}^{N_{test}} |\lambda_k^{(i)} - \bar{\lambda}_k|^2},$$

where $\bar{\lambda}_k$ is the mean of the ground truth eigenvalues. R^2 indicates how well the model captures the variability of the eigenvalues with respect to parameter changes.

- **Mean Absolute Percentage Error (MAPE):** Measures the relative accuracy.

$$(5.3) \quad \text{MAPE}_k = \frac{1}{N_{test}} \sum_{i=1}^{N_{test}} \frac{|\lambda_k^{(i)} - \hat{\lambda}_k^{(i)}|}{|\lambda_k^{(i)}|} \times 100\%.$$

This metric provides a scale-independent assessment, which is particularly useful given that high-frequency eigenvalues typically have larger magnitudes.

2. *Eigensubspace Metrics.* Evaluating the quality of the predicted subspace \mathcal{U} (spanned by \mathbf{Q}_U) against the target subspace \mathcal{V} (spanned by \mathbf{Q}_V) is crucial, as it determines the success of the subsequent Rayleigh-Ritz reconstruction.

- **Subspace Loss (\mathcal{L}_1):** As defined in Eq. (3.9), this metric serves as the training objective and quantifies the alignment of the orthonormal bases.
- **Projection Distance (d_{pr}):** Defined as the spectral norm of the difference between projection matrices:

$$(5.4) \quad d_{pr}(\mathcal{U}, \mathcal{V}) = \|\mathbf{P}_U - \mathbf{P}_V\|_2 = \sin(\theta_{\max}),$$

where θ_{\max} is the largest principal angle between the subspaces. This metric captures the *worst-case* misalignment direction between the predicted and true subspaces.

- **Chordal Distance (d_{ch}):** Defined using the Frobenius norm:

$$(5.5) \quad d_{ch}(\mathcal{U}, \mathcal{V}) = \frac{1}{\sqrt{2}} \|\mathbf{P}_U - \mathbf{P}_V\|_F = \sqrt{\sum_j \sin^2(\theta_j)}.$$

This metric provides an aggregate measure of the distance, accounting for deviations across all dimensions of the subspace.

3. *Eigenfunction Reconstruction Metrics.* Directly comparing a predicted eigenfunction \tilde{u}_k with the ground truth u_k is problematic in non-selfadjoint problems due to mode switching and index shifting near eigenvalue crossings. The indices of eigenvalues sorted by modulus may swap due to small perturbations, making index-to-index comparison unreliable.

L_1	d_{pr}	d_{ch}
1.65×10^{-5}	0.0020	0.0040

Table 2: Prediction error of eigensubspaces.

Instead, we adopt a projection-based evaluation strategy. We assess how well the *true* eigenfunction u_k can be represented by the predicted subspace \mathcal{U} . If u_k lies almost entirely within \mathcal{U} , then the Rayleigh-Ritz procedure will accurately recover it, regardless of its index. Let u_k be the ground truth eigenfunction and $\mathcal{P}_{\mathcal{U}}u_k = \mathbf{Q}_{\mathcal{U}}\mathbf{Q}_{\mathcal{U}}^H u_k$ be its projection onto the predicted subspace. We use:

- **Maximum Absolute Error (MaxAE):**

$$(5.6) \quad \text{MaxAE}_k = \max_{x \in \Omega} |(u_k - \mathcal{P}_{\mathcal{U}}u_k)(x)|.$$

This measures the worst-case pointwise approximation error, ensuring no local singularities or artifacts are missed. Noted that the eigenfunctions are scaled to the same norm.

- **Cosine Similarity (CS):**

$$(5.7) \quad \text{CS}_k = \frac{|\langle u_k, \mathcal{P}_{\mathcal{U}}u_k \rangle|}{\|u_k\|_2 \|\mathcal{P}_{\mathcal{U}}u_k\|_2}.$$

CS measures the directional alignment. A value close to 1 indicates that the true eigenfunction is nearly parallel to the predicted subspace.

- **Relative L^1 Error (RelL1):**

$$(5.8) \quad \text{RelL1}_k = \frac{\|u_k - \mathcal{P}_{\mathcal{U}}u_k\|_1}{\|u_k\|_1}.$$

The L^1 norm imposes a stricter penalty on small, distributed errors compared to the L^2 norm, promoting sparsity in the residual and ensuring global structural fidelity.

Justification for Projection-based Metrics for Eigenfunctions: From the perspective of Galerkin methods, the accuracy of the approximate solution depends solely on the approximation property of the trial subspace \mathcal{U} . As long as the true solution u_k resides "close" to \mathcal{U} (i.e., the projection residual $\|(I - \mathcal{P}_{\mathcal{U}})u_k\|$ is small), the Rayleigh-Ritz procedure is mathematically guaranteed to find a Ritz vector \tilde{u} that converges to u_k . Therefore, verifying the inclusion of u_k in \mathcal{U} is theoretically sufficient and more robust than verifying individual vector matches.

5.2. Numerical Results. In this subsection, we present the experimental results obtained on the square domain $\Omega = [0, 1]^2$. The target output consists of the eigensubspace spanned by the first 12 eigenfunctions, which covers the first five complete eigenvalue clusters. This setup challenges the network to capture high-frequency spectral dependencies and disentangle closely spaced eigenvalues.

We first evaluate the quality of the predicted eigensubspace \mathcal{U} , as this is the cornerstone of our proposed framework. Table 5.2 summarizes the prediction errors on the test set using the three metrics defined in the previous section.

The quantitative results in Table 5.2 demonstrate the exceptional accuracy of the DEN architecture in learning the parameter-to-eigensubspace mapping. The test

Eigen Index	Eigenvalue			Eigenfunction		
	MAE	R^2	MAPE / %	MaxAE	CS	RelL1
1	0.0009	0.9987	0.1093	0.0066	1.0000	0.0012
2	0.0009	0.9988	0.1073	0.0063	1.0000	0.0011
3	0.0003	0.9999	0.0249	0.0058	1.0000	0.0011
4	0.0074	0.9987	0.3247	0.0066	1.0000	0.0011
5	0.0007	0.9999	0.0233	0.0073	1.0000	0.0013
6	0.0007	0.9999	0.0236	0.0074	1.0000	0.0013
7	0.0004	1.0000	0.0133	0.0070	1.0000	0.0013
8	0.0004	1.0000	0.0142	0.0074	1.0000	0.0013
9	0.0002	1.0000	0.0039	0.0083	1.0000	0.0018
10	0.0002	1.0000	0.0034	0.0092	1.0000	0.0018
11	0.0002	1.0000	0.0033	0.0068	1.0000	0.0016
12	0.0002	1.0000	0.0037	0.0083	1.0000	0.0019

Table 3: Prediction error of eigenvalues and eigenfunctions. The horizon lines splits eigenvalues and eigenfunctions into clusters.

loss \mathcal{L}_1 converges to a magnitude of 10^{-5} , indicating effective generalization to unseen refractive index profiles. Geometrically, the projection distance of $d_{pr} \approx 0.0020$ corresponds to a maximum principal angle of merely 0.11° , rendering the predicted subspace \mathcal{U} nearly indistinguishable from the true invariant subspace \mathcal{V} in terms of orientation. Furthermore, the low chordal distance ($d_{ch} \approx 0.0040$) guarantees negligible projection errors for the subsequent Rayleigh-Ritz reconstruction, thereby validating our core hypothesis: while individual eigenvectors may be numerically unstable due to non-selfadjointness, the underlying eigensubspace is robust and can be learned with high precision.

Table 5.2 presents the quantitative errors of the 12 eigenpairs reconstructed via the Rayleigh-Ritz method, based on the predicted eigensubspace. The horizontal lines in the table demarcate the five distinct eigenvalue clusters identified in the spectrum: $\{1, 2\}$, $\{3\}$, $\{4\}$, $\{5, 6, 7, 8\}$, and $\{9, 10, 11, 12\}$.

- **Eigenvalue Accuracy and Spectral Consistency:** The reconstruction accuracy remains consistently high across the entire spectrum. While the decrease in MAPE for higher indices (Indices 9-12) is expected due to the increasing magnitude of the eigenvalues, the most significant indicator of model performance is the stability of MAE. Despite the increasing complexity and oscillatory nature of the eigenfunctions for higher modes, the MAE remains at a very low level ($\sim 10^{-4}$) without exhibiting significant degradation. This suggests that the DEN architecture successfully mitigates the "spectral pollution" or dispersion errors often encountered in high-frequency approximations. Furthermore, the near-perfect R^2 scores (> 0.999) for the high-frequency clusters indicate that the model effectively captures the parameter-dependence of these modes, accurately predicting how minute variations in the refractive index $n(x)$ modulate the spectrum.
- **Robustness to Clustering:** The method demonstrates remarkable robustness in resolving spectral structures, regardless of whether the eigenvalues appear in isolation or form dense clusters.
 - **Isolated Modes (Indices 3 & 4):** The algorithm handles isolated

eigenvalues with high fidelity. For instance, Index 4 exhibits a slightly elevated MAE (0.0074), which is a typical outlier likely due to specific parameter sensitivity in that spectral region. However, the corresponding eigenfunction fidelity remains excellent (CS = 1.0000), proving that the predicted subspace is correctly aligned with the target direction, and the scalar deviation is numerically bounded.

- **Dense Clusters (Indices 5-8 & 9-12):** A key challenge in non-selfadjoint problems is the instability of individual eigenpairs within dense clusters. For the 4-fold clusters at indices 5-8 and 9-12, our method achieves exceptional accuracy (e.g., $R^2 \approx 1.0000$ for Indices 9-12). This validates the theoretical assertion in Section 4.1: while the intra-cluster eigenvalues are sensitive to perturbations, the total invariant subspace they span is stable. By accurately learning this stable subspace, the subsequent Rayleigh-Ritz procedure acts as a robust local solver, effectively resolving the internal fine structure of the clusters and disentangling the crossing modes.
- **Eigenfunction Fidelity:** The eigenfunction reconstruction is exceptionally stable. The Cosine Similarity (CS) remains at 1.0000 across all 12 modes, implying near-perfect directional alignment. The pointwise errors (MaxAE) show a slight, expected increase for the highest frequency cluster (Indices 9-12, MaxAE ≈ 0.009) compared to the lowest modes (MaxAE ≈ 0.006). This marginal increase is attributable to the more complex oscillatory nature of high-frequency eigenfunctions, which naturally pose a greater challenge for pointwise approximation. However, the consistently low RelL1 errors (< 0.002) confirm that the global structural integrity of the eigenfunctions is preserved for all clusters.

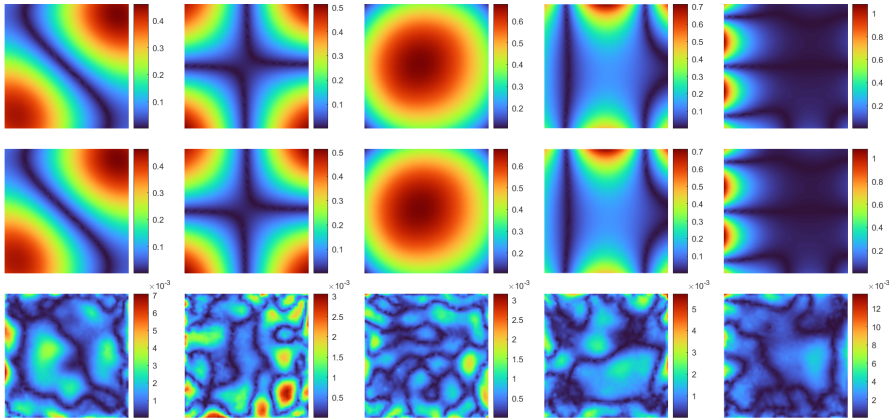
Figure 3 provides a qualitative assessment of the subspace prediction quality. We visualize the eigenfunctions corresponding to indices 1, 3, 4, 5, and 9, which serve as representatives for the five distinct eigenvalue clusters identified in the spectrum.

Visual Inspection: As illustrated in the top two rows, the projected eigenfunctions ($\mathcal{P}_{\mathcal{U}}u_k$) are visually indistinguishable from the ground truth (u_k) for both real and imaginary components. This confirms that the predicted subspace \mathcal{U} successfully captures the dominant geometric features and oscillating patterns of the true eigenfunctions.

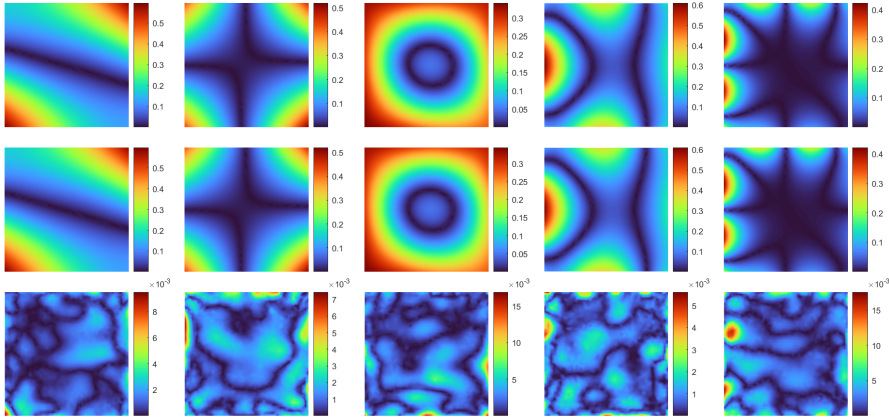
Error Distribution: The pointwise relative error maps (bottom row) quantify this similarity, revealing that the discrepancy is strictly controlled, with maximum error magnitudes remaining on the order of 10^{-3} .

Cluster-Dependent Performance: A subtle but noteworthy observation is that the projection errors for eigenfunctions within dense clusters (e.g., Indices 5 and 9) are marginally higher than those for isolated low-frequency modes (e.g., Index 3). This is possibly because isolated eigenvalues correspond to 1D invariant subspaces, whereas clusters correspond to multi-dimensional subspaces (e.g., 4D for Index 9). Learning the precise orientation of a higher-dimensional hyperplane naturally presents a greater challenge than identifying a single vector direction.

5.3. Generalization via Subspace Interpolation on New Meshes. To balance computational efficiency with practical utility, the model was trained on a relatively coarse discretization to predict the eigensubspace $V \in \mathbb{R}^{M_0 \times K}$. However, practical applications often demand solutions on arbitrary or higher-resolution grids with mesh size M_1 . To evaluate the generalization capability of the predicted sub-



(a) Real part of eigenfunctions (top), their projection onto the predicted eigensubspace (middle) and relative errors (bottom).



(b) Imaginary part of eigenfunctions (top), their projection onto the predicted eigensubspace (middle) and relative errors (bottom).

Fig. 3: Visualization of predicted eigensubspace.

space, we examine its performance when interpolated onto target meshes of varying resolutions: one with a resolution comparable to the training grid, and a finer mesh with a grid size half that of the original. As a baseline for comparison, we also evaluate the performance of the ground truth subspace from the original coarse mesh interpolated onto these target domains.

We focus on the first 12 eigenmodes on a square domain. The evaluation metrics include the Mean Absolute Error (MAE) for eigenvalues and the relative projection error for eigenfunctions, defined as $\|(I - P_V)u_k\|/\|u_k\|$, where P_V denotes the orthogonal projection matrix of the interpolated subspace and u_k represents the k -th ground truth eigenfunction on the target mesh. Furthermore, the global quality of

the subspace alignment is quantified using the chordal distance, denoted as d_{ch} .

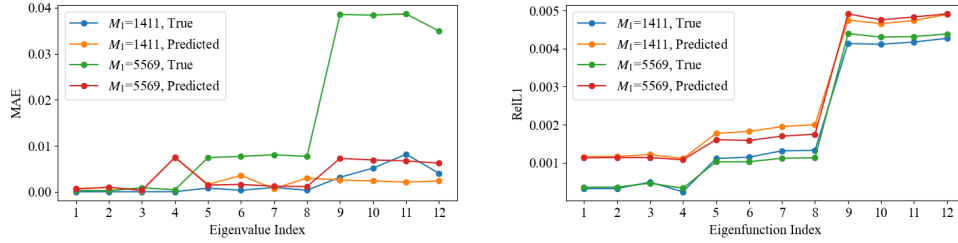


Fig. 4: Interpolation error of eigenvalues and eigenfunctions

Figure 4 illustrates the error profiles for eigenvalues and eigenfunctions. A general trend is observed where errors increase with the spectral order k , and interpolation onto the finer mesh yields higher errors compared to the comparable mesh. Notably, regarding eigenvalues, the error between the ground truth eigenvalues of the original mesh and those of the target mesh is larger than the error obtained using the interpolated predicted subspace. This can be attributed to the Rayleigh-Ritz procedure applied to the predicted subspace, which effectively incorporates the geometric and operator information of the fine-grid discretization, thereby refining the eigenvalue estimates. In terms of eigenfunctions, the projection error similarly correlates with spectral order and mesh resolution. However, unlike the eigenvalue case, the interpolated predicted subspace exhibits projection errors that are quantitatively comparable to those of the interpolated ground truth subspace, suggesting that the model captures the underlying spectral structure as robustly as the numerical ground truth.

M_1	1411		5569	
T / P	P	T	P	T
d_{ch}	0.0122	0.0109	0.0098	0.0106

Table 4: Interpolation error of eigen subspaces. "T" represents interpolation of true eigenfunction; "P" represents interpolation of predicted eigen subspace.

Table 5.3 presents the chordal distance d_{ch} between the true subspace on the target mesh and the interpolated subspaces derived from both the prediction and the coarse-grid ground truth. The errors decrease slightly on the finer mesh and the discrepancy between the predicted and ground truth methods remains negligible. This confirms that the predicted subspace retains high fidelity even after interpolation to significantly finer discretizations.

Figure 5 visualizes the eigenfunctions corresponding to indices 1, 3, 4, 5, and 9 on the refined mesh, representing the leading modes of the first five eigenvalue clusters. It displays the ground truth eigenfunctions, their projections onto the subspace interpolated from the model prediction, and the spatial distribution of the relative projection errors. Visually, the projected eigenfunctions exhibit high fidelity to the ground truth, with the error magnitudes remaining negligible. Notably, the error distribution follows a scale-like pattern, indicating that the error localization correlates with the sampling points and the geometric deviation relative to the original coarse

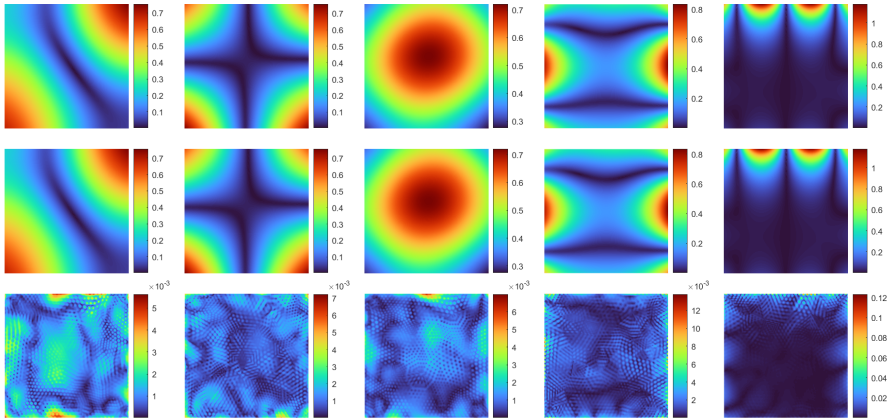


Fig. 5: Modulus of eigenfunctions (top), their projection onto the subspace interpolated from the model prediction (middle) and relative errors (bottom).

mesh. These results further corroborate the validity of the predicted subspace even after interpolation onto finer discretizations.

5.4. Robustness Analysis across Varying Wavenumbers. In the preceding experiments, the wavenumber was fixed at $k = 1$. However, varying k fundamentally alters the spectral properties of the Steklov problem. When k is small, the problem can be viewed as a perturbation of the Laplace-Steklov problem, where symmetries in the domain (e.g., the square domain) lead to degenerate eigenvalues that split into tight clusters under the perturbation of $k^2 n(x)$. As k increases, these clusters tend to dissolve as the spectrum spreads. More critically, the increase in wavenumber leads to a densification of the spectrum, causing the uniform spectral isolation assumption (Assumption 4.3) to fail. In this high-frequency regime, it becomes impossible to define a fixed contour that consistently encloses exactly the top K eigenvalues for all samples without external modes crossing the boundary. Consequently, the mapping from parameters to the exact K -dimensional eigensubspace becomes discontinuous due to frequent mode switching.

To address this challenge, we leverage the concept of subspace embedding[15]. Instead of attempting to predict the exact, potentially discontinuous K -dimensional target space, we train the network to predict a higher-dimensional subspace $\mathcal{U}_{K_{out}}$ with $K_{out} > K$. The rationale is that this larger "ansatz space" can encompass the union of all dominant eigenfunctions that might fluctuate into the range of interest across the parameter distribution. The subsequent Rayleigh-Ritz procedure then serves as a robust filter to extract the best K eigenpairs from this enriched subspace.

We evaluate the model's robustness under varying squared wavenumbers $k^2 \in \{0.25, 1, 4, 10\}$. For the lower-frequency regimes ($k^2 = 0.25, 1$), where spectral isolation holds, we set the output dimension equal to the target dimension ($K_{out} = K = 12$). For the higher-frequency regimes ($k^2 = 4, 10$), where mode mixing is expected, we employ the embedding strategy with increased output dimensions of $K_{out} = 24$ and $K_{out} = 48$, respectively.

Figure 6 illustrates the performance trends of representative metrics (Eigenvalue MAE, Eigenfunction ReL1, and Subspace Chordal Distance) as the wavenumber in-

creases. We observe a general trend of performance degradation across all metrics as k^2 grows. This is anticipated, as higher wavenumbers correspond to more oscillatory eigenfunctions, which naturally pose greater challenges for both the neural operator and the finite element ground truth generation. However, despite the relative degradation, the absolute error magnitudes remain satisfactory even for the challenging $k^2 = 10$ case, with the eigenvalue MAE maintained around the 10^{-2} level, suggesting that the method retains practical utility in higher frequency regimes.

To further validate the necessity of the embedding strategy, Figure 7 details the impact of the output subspace dimension K_{out} on model performance for the specific case of $k^2 = 10$. The results show a clear monotonic improvement in accuracy as K_{out} increases from 12 to 48. This empirical evidence confirms that a larger predicted subspace effectively accommodates the "mode switching" phenomenon at the boundary of the target spectrum, capturing necessary spectral information that would otherwise be lost if the network were constrained to a fixed K -dimensional output. We note that experiments for significantly higher wavenumbers ($k^2 \gg 10$) are currently omitted, as the standard FEM ground truth generation begins to suffer from non-negligible numerical dispersion errors in such highly oscillatory regimes.

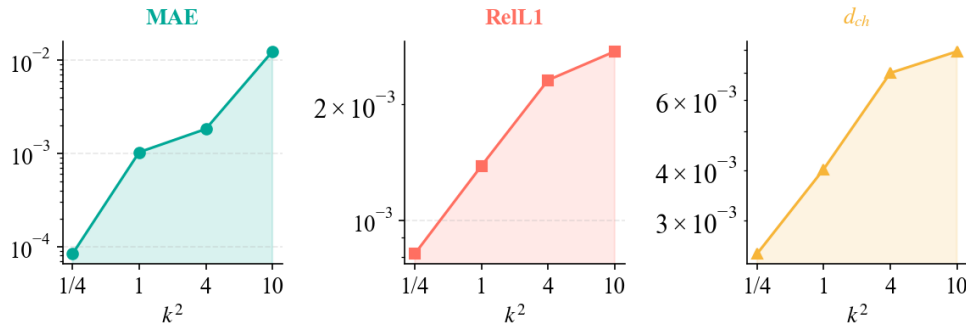


Fig. 6: Performance trends of DEN across varying wavenumbers $k^2 \in \{0.25, 1, 4, 10\}$. Metrics shown are Eigenvalue MAE (averaged over top 12), Eigenfunction RelL1 (averaged), and Subspace Chordal Distance d_{ch} . Subspace embedding ($K_{out} > 12$) is employed for $k^2 \geq 4$.

5.5. Ablation Study. To rigorously validate the effectiveness of the proposed architectural components—specifically the geometry-adaptive POD basis and the low-rank banded cross-mode mixing—we conduct a series of ablation studies. We compare the full **DEN** model against several variants and baselines. The results are summarized in Table 5.

Impact of Basis Selection. We first evaluate the influence of the spectral basis Ψ on reconstruction accuracy. The results demonstrate that the proposed target-derived basis, $\text{POD}(\mathbf{Y})$, significantly outperforms the geometry-driven graph Laplacian basis (DEN-Lap), reducing the MAE from 2.25 to 1.03. While the Laplacian basis generalizes well to the domain geometry, the POD basis optimally encodes the specific energy spectrum of the Steklov eigenfunctions, confirming the theoretical optimality discussed in Section 2.3. We also experimented with a basis derived from the joint input-output snapshot matrix (DEN-XY), which yielded slightly inferior performance compared to using $\text{POD}(\mathbf{Y})$ alone. This indicates that incorporating input features

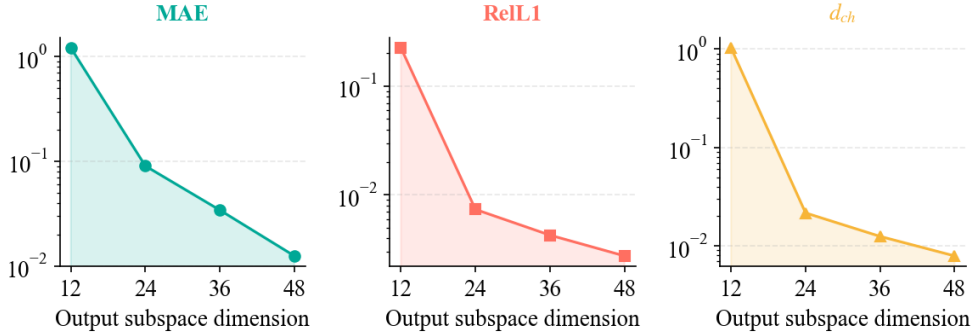


Fig. 7: Impact of output subspace dimension K_{out} on model performance for the high-frequency case $k^2 = 10$. Increasing the embedding dimension effectively mitigates errors caused by spectral crossing at the boundary of the range of interest.

Table 5: Ablation study and baseline comparison. **DEN** denotes the proposed model using $\text{POD}(\mathbf{Y})$ basis and Low-Rank Banded mixing. **DEN-BFR**: Banded mixing without low-rank constraint. **DEN-Dense**: Global mixing without banded or low-rank constraints. **DEN-Diag**: No cross-mode mixing (diagonal only). **DEN-XY**: Uses joint POD basis of inputs and outputs (equivalent to PODNO with mixing). **DEN-Lap**: Uses Graph Laplacian eigenfunctions as basis (equivalent to G-FuNK with mixing). **PODNO/G-FuNK**: Standard baselines without mixing mechanisms. **FNO**: Standard Fourier Neural Operator with interpolation.

Model	MAE ($\times 10^{-3}$)	ReL1 ($\times 10^{-3}$)	d_{ch} ($\times 10^{-3}$)	Params
DEN	1.0324	1.3839	4.0260	2,200,536
DEN-BFR	1.8937	1.5522	4.5110	2,488,536
DEN-Dense	1.0514	1.8356	5.5449	2,488,536
DEN-Diag	2.1927	2.2502	6.5927	2,027,736
DEN-XY	1.0334	1.5946	4.6279	2,200,536
DEN-Lap	2.2530	2.3331	6.8763	2,200,536
PODNO	2.7347	2.7719	8.1112	2,200,536
G-FuNK	3.7542	3.1976	9.3496	2,200,536
FNO	7.4960	4.7606	14.0322	7,135,305

(refractive index) into the basis construction likely introduces unnecessary noise to the output space representation, as the primary objective is to span the solution manifold rather than the parameter manifold. Furthermore, the standard FNO, which necessitates interpolation onto a uniform grid, exhibits the highest error (7.49). This sharp contrast underscores the superiority of our mesh-agnostic spectral approach over methods constrained by FFT requirements and interpolation artifacts.

Importance of Cross-Mode Mixing. Next, we investigate the necessity of the proposed cross-mode mixing mechanism. The variant without mixing (DEN-Diag) exhibits a substantial increase in error compared to the full DEN (MAE: 2.19 vs.

1.03). Similarly, standard spectral baselines lacking explicit mixing, such as PODNO and G-FuNK, perform significantly worse. These results confirm our hypothesis that the diagonal assumption inherent in standard spectral layers is insufficient for non-selfadjoint operators, where strong spectral coupling exists.

Regarding the efficiency of the mixing strategy, we compared our Low-Rank Banded approach against two denser alternatives: full-rank banded mixing (DEN-BFR) and unconstrained global mixing (DEN-Dense). Interestingly, the proposed DEN outperforms both heavier variants. The unconstrained DEN-Dense likely suffers from optimization difficulties or overfitting due to the excessive parameterization of spectral interactions. By enforcing a banded low-rank structure, DEN not only reduces the parameter count (saving ~ 0.3 million parameters compared to the full rank settings) but also imposes a beneficial inductive bias that focuses on physically relevant, local spectral interactions. In summary, the proposed DEN achieves the best trade-off between accuracy and model complexity.

6. Conclusions and Discussions. In this work, we addressed the challenging problem of spectral inference for parametric non-selfadjoint Steklov eigenvalue problems. We proposed the Deep Eigenspace Network (DEN), a specialized architecture that advances the standard Fourier Neural Operator framework through improvements in mesh adaptability, optimal basis selection in the frequency domain, and explicit cross-mode interactions.

To overcome the inherent discontinuity of individual eigenfunctions caused by spectral crossings and non-selfadjointness, our methodology shifts from direct eigenfunction regression to invariant subspace learning. By predicting the stable eigensubspace spanned by the target cluster and subsequently employing the Rayleigh-Ritz procedure, we robustly recover the eigenvalues and eigenfunctions with high fidelity.

Theoretically, we established the well-posedness of this learning framework. We proved that for the considered spectral range (the first $k = 12$ eigenvalues), a uniform contour exists such that the resolvent remains bounded for all admissible parameters. Building on this uniform stability, we proved the Lipschitz continuous dependence of the eigensubspace on the parameters and derived explicit upper bounds for the eigenvalue reconstruction error. Numerically, our experiments demonstrate that DEN achieves exceptional accuracy in subspace prediction. Furthermore, the method exhibits strong zero-shot generalization capabilities across different mesh resolutions, validating its discretization-independent nature. These results characterize DEN as a fast, accurate, and flexible surrogate solver. Furthermore, we empirically examined the impact of the wavenumber k on the model’s performance. Our results indicate that the proposed method yields highly accurate predictions in the low-wavenumber limit. Moreover, even in high-wavenumber regimes where spectral instability increases, we demonstrated that satisfactory reconstruction fidelity can be effectively preserved by employing a subspace embedding strategy to accommodate the expanded spectral content.

The proposed framework holds significant promise for downstream applications, including the construction of enrichment basis functions for Generalized Finite Element Methods (GFEM), Model Order Reduction (MOR) for large-scale PDE systems, and accelerating forward solvers in inverse scattering problems.

Limitations and Future Work. The theoretical efficacy of our method relies on the Assumption 4.3. As demonstrated in our numerical experiments with varying wavenumbers, this assumption is inevitably compromised in high-frequency regimes where the spectrum becomes dense. While our experiments confirmed that the sub-

space embedding strategy effectively mitigates the impact of mode mixing and preserves prediction accuracy by encompassing a larger spectral window, this approach faces scalability challenges in the high-frequency limit. As the wavenumber k increases further, the dimension of the required embedding subspace may grow significantly, potentially offsetting the computational efficiency of the reduced-order model. Moreover, generating reliable ground truth data for extremely high-frequency problems remains a bottleneck in standard Finite Element Methods. Future research will focus on developing adaptive basis sizing strategies and integrating asymptotic high-frequency theories to extend the applicability of DEN to these extreme regimes.

REFERENCES

- [1] J. AN, H. BI, AND Z. LUO, *A highly efficient spectral-galerkin method based on tensor product for fourth-order steklov equation with boundary eigenvalue*, Journal of Inequalities and Applications, 2016 (2016), p. 211.
- [2] A. B. ANDREEV AND T. D. TODOROV, *Isoparametric finite-element approximation of a steklov eigenvalue problem*, IMA journal of numerical analysis, 24 (2004), pp. 309–322.
- [3] Z. BAI, J. DEMMEL, J. DONGARRA, A. RUHE, AND H. VAN DER VORST, *Templates for the solution of algebraic eigenvalue problems: a practical guide*, SIAM, 2000.
- [4] I. BEN-SHAUL, L. BAR, D. FISHELOV, AND N. SOCHEN, *Deep learning solution of the eigenvalue problem for differential operators*, Neural Computation, 35 (2023), pp. 1100–1134.
- [5] H. BI, H. LI, AND Y. YANG, *An adaptive algorithm based on the shifted inverse iteration for the steklov eigenvalue problem*, Applied Numerical Mathematics, 105 (2016), pp. 64–81.
- [6] J. H. BRAMBLE AND J. OSBORN, *Approximation of steklov eigenvalues of non-selfadjoint second order elliptic operators*, in The mathematical foundations of the finite element method with applications to partial differential equations, Elsevier, 1972, pp. 387–408.
- [7] F. CAKONI, D. COLTON, S. MENG, AND P. MONK, *Stekloff eigenvalues in inverse scattering*, SIAM journal on applied mathematics, 76 (2016), pp. 1737–1763.
- [8] J. CANAVATI AND A. A. MINZONI, *A discontinuous steklov problem with an application to water waves*, Journal of Mathematical Analysis and Applications, 69 (1979), pp. 540–558.
- [9] L. CAO, L. ZHANG, W. ALLEGRETTO, AND Y. LIN, *Multiscale asymptotic method for steklov eigenvalue equations in composite media*, SIAM Journal on Numerical Analysis, 51 (2013), pp. 273–296.
- [10] Y. CHANG, O. BENCHEKROUN, M. M. CHIARAMONTE, P. YICHEN CHEN, AND E. GRINSPUN, *Neural representation of shape-dependent laplacian eigenfunctions*, arXiv e-prints, (2024), pp. arXiv-2408.
- [11] Z. CHENG, Z. WANG, L.-L. WANG, AND M. AZAIEZ, *Podno: Proper orthogonal decomposition neural operators*, arXiv preprint arXiv:2504.18513, (2025).
- [12] G. CORSO, H. STARK, S. JEGELKA, T. JAAKKOLA, AND R. BARZILAY, *Graph neural networks*, Nature Reviews Methods Primers, 4 (2024), p. 17.
- [13] X. DAI, Y. FAN, AND Z. SHENG, *Subspace method based on neural networks for eigenvalue problems*, arXiv preprint arXiv:2410.13358, (2024).
- [14] C. ECKART AND G. YOUNG, *The approximation of one matrix by another of lower rank*, Psychometrika, 1 (1936), pp. 211–218.
- [15] V. FANASKOV, V. TRIFONOV, A. RUDIKOV, E. MURAVLEVA, AND I. OSELEDETS, *Deep learning for subspace regression*, arXiv preprint arXiv:2509.23249, (2025).
- [16] J. HAN, J. LU, AND M. ZHOU, *Solving high-dimensional eigenvalue problems using deep neural networks: A diffusion Monte Carlo like approach*, Journal of Computational Physics, 423 (2020), p. 109792.
- [17] X. HAN, Y. LI, AND H. XIE, *A multilevel correction method for steklov eigenvalue problem by nonconforming finite element methods*, Numerical Mathematics: Theory, Methods and Applications, 8 (2015), pp. 383–405.
- [18] X. JI, Y. JIAO, X. LU, P. SONG, AND F. WANG, *Deep Ritz method for elliptical multiple eigenvalue problems*, Journal of Scientific Computing, 98 (2024), p. 48.
- [19] N. KUZNETSOV, T. KULCZYCKI, M. KWASNICKI, A. NAZAROV, S. POBORCHI, I. POLTEROVICH, AND B. SIUDEJA, *The legacy of vladimir andreevich steklov*, Notices of the AMS, 61 (2014), p. 190.
- [20] H. LI, J. SUN, AND Z. ZHANG, *Operator inference for elliptic eigenvalue problems*, arXiv preprint arXiv:2504.15733, (2025).

- [21] H. LI AND L. YING, *A semigroup method for high dimensional elliptic PDEs and eigenvalue problems based on neural networks*, Journal of Computational Physics, 453 (2022), p. 110939.
- [22] Z. LI, N. KOVACHKI, K. AZIZZADENESHELI, B. LIU, K. BHATTACHARYA, A. STUART, AND A. ANANDKUMAR, *Fourier neural operator for parametric partial differential equations*, arXiv preprint arXiv:2010.08895, (2020).
- [23] Z. LI, N. KOVACHKI, K. AZIZZADENESHELI, B. LIU, K. BHATTACHARYA, A. STUART, AND A. ANANDKUMAR, *Neural operator: Graph kernel network for partial differential equations*, arXiv preprint arXiv:2003.03485, (2020).
- [24] Z. LI, N. KOVACHKI, K. AZIZZADENESHELI, B. LIU, A. STUART, K. BHATTACHARYA, AND A. ANANDKUMAR, *Multipole graph neural operator for parametric partial differential equations*, Advances in Neural Information Processing Systems, 33 (2020), pp. 6755–6766.
- [25] J. LIU, J. SUN, AND T. TURNER, *Spectral indicator method for a non-selfadjoint steklov eigenvalue problem*, Journal of Scientific Computing, 79 (2019), pp. 1814–1831.
- [26] Z. LIU, H. WANG, H. ZHANG, K. BAO, X. QIAN, AND S. SONG, *Render unto numerics: Orthogonal polynomial neural operator for pdes with nonperiodic boundary conditions*, SIAM Journal on Scientific Computing, 46 (2024), pp. C323–C348.
- [27] S. E. LOEFFLER, Z. AHMAD, S. Y. ALI, C. YAMAMOTO, D. M. POPESCU, A. YEE, Y. LAL, N. TRAYANOVA, AND M. MAGGIONI, *Graph fourier neural kernels (g-funk): Learning solutions of nonlinear diffusive parametric pdes on multiple domains*, arXiv preprint arXiv:2410.04655, (2024).
- [28] L. LU, P. JIN, AND G. E. KARNIADAKIS, *Deeponet: Learning nonlinear operators for identifying differential equations based on the universal approximation theorem of operators*, arXiv preprint arXiv:1910.03193, (2019).
- [29] D. MORA, G. RIVERA, AND R. RODRÍGUEZ, *A virtual element method for the steklov eigenvalue problem*, Mathematical Models and Methods in Applied Sciences, 25 (2015), pp. 1421–1445.
- [30] A. D. RUSSO AND A. E. ALONSO, *A posteriori error estimates for nonconforming approximations of steklov eigenvalue problems*, Computers & Mathematics with Applications, 62 (2011), pp. 4100–4117.
- [31] Y. SAAD, *Numerical methods for large eigenvalue problems: revised edition*, SIAM, 2011.
- [32] G. W. STEWART AND J.-G. SUN, *Matrix Perturbation Theory*, Computer Science and Scientific Computing, Academic Press, Boston, 1990.
- [33] J. SUN AND A. ZHOU, *Finite element methods for eigenvalue problems*, CRC Press, Boca Raton, FL, 2016.
- [34] Y. WANG AND H. XIE, *Computing multi-eigenpairs of high-dimensional eigenvalue problems using tensor neural networks*, Journal of Computational Physics, 506 (2024), p. 112928.
- [35] Z. WANG, J. XIN, AND Z. ZHANG, *DeepParticle: learning invariant measure by a deep neural network minimizing wasserstein distance on data generated from an interacting particle method*, Journal of Computational Physics, 464 (2022), p. 111309.